A Catalog of Quasar Properties from SDSS DR7

Yue Shen[1], Gordon T. Richards[2], Michael A. Strauss[3], Patrick B. Hall[4], Donald P. Schneider[5], Stephanie Snedden[6], Dmitry Bizyaev[6], Howard Brewington[6], Viktor Malanushenko[6], Elena Malanushenko[6], Dan Oravetz[6], Kaike Pan[6], Audrey Simmons[6]

ABSTRACT

We present a compilation of properties of the 105,783 quasars in the SDSS Data Release 7 (DR7) quasar catalog. In this product, we compile continuum and emission line measurements around the Hα, Hβ, Mg II and C IV regions, as well as other quantities such as radio properties, and flags indicating broad absorption line quasars (BALQSOs), disk emitters, etc. We also compile virial black hole mass estimates based on various calibrations. For the fiducial virial mass estimates we use the Vestergaard & Peterson (VP06) calibrations for Hβ and C IV, and our own calibration for Mg II which matches the VP06 Hβ masses on average. We describe the construction of this catalog, and discuss its limitations. The catalog and its future updates will be made publicly available online.

Subject headings: black hole physics — galaxies: active — quasars: general — surveys

1. Introduction

In recent years, studies of quasars and active galactic nuclei (AGNs) have been greatly facilitated by dedicated large-scale wide and deep field surveys in different bands, most notably by optical surveys such as the Sloan Digital Sky Survey (SDSS, York et al. 2000) and

[1]Harvard-Smithsonian Center for Astrophysics, 60 Garden St., MS-51, Cambridge, MA 02138, USA.

[2]Department of Physics, Drexel University, 3141 Chestnut Street, Philadelphia, PA 19104, USA.

[3]Princeton University Observatory, Princeton, NJ 08544, USA.

[4]Dept. of Physics & Astronomy, York University, 4700 Keele St., Toronto, ON, M3J 1P3, Canada.

[5]Department of Astronomy and Astrophysics, 525 Davey Laboratory, Pennsylvania State University, University Park, PA 16802, USA.

[6]Apache Point Observatory, Sunspot, NM, 88349, USA.

the 2QZ survey (Croom et al. 2004). Indeed, the growing body of data has revolutionized the study of quasars and AGNs. Large, homogeneous data sets allow detailed investigations of the phenomenological properties of quasars and AGNs, offering new insights into the central engine powering these objects and their connections to their host galaxies, especially when combined with multi-wavelength coverage. At the same time, it has become important to fit the quasar/AGN population into its cosmological context, i.e., how the supermassive black hole (SMBH) population evolves across cosmic time. These data have led to a coherent picture of the cosmic evolution of the SMBH population within the concordance ΛCDM paradigm (Kauffmann & Haehnelt 2000; Wyithe & Loeb 2003; Hopkins et al. 2006, 2008; Shankar et al. 2009; Shen 2009), where the key observational components include quasar clustering, the luminosity function (LF), the BH mass function, and the correlations between BHs and their host properties. Increasingly larger data sets are offering unique opportunities to measure these properties with unprecedented precision.

In an earlier study of the virial BH mass and Eddington ratio distributions of quasars, we measured spectral properties for the SDSS Data Release 5 (DR5) quasar catalog (Schneider et al. 2007; Shen et al. 2008b). We hereby extend this exercise to the DR7 quasar catalog (Schneider et al. 2010). We now include a more complete compilation than before of quantities from our spectral fits. Our measurements are more sophisticated than the SDSS pipeline outputs in many ways, and are hence of practical value. We describe the parent quasar sample in §2, and the spectral measurements and the catalog format in §3. We discuss possible applications of our measurements in §4. Throughout this paper we use cosmological parameters $\Omega_\Lambda = 0.7$, $\Omega_0 = 0.3$ and $h = 0.7$.

2. The Sample

The SDSS uses a dedicated 2.5-m wide-field telescope (Gunn et al. 2006) with a drift-scan camera with 30 2048×2048 CCDs (Gunn et al. 1998) to image the sky in five broad bands ($u\,g\,r\,i\,z$; Fukugita et al. 1996). The imaging data are taken on dark photometric nights of good seeing (Hogg et al. 2001), are calibrated photometrically (Smith et al. 2002; Ivezić et al. 2004; Tucker et al. 2006) and astrometrically (Pier et al. 2003), and object parameters are measured (Lupton et al. 2001; Stoughton et al. 2002). Quasar candidates (Richards et al. 2002a) for follow-up spectroscopy are selected from the imaging data using their colors, and are arranged in spectroscopic plates (Blanton et al. 2003) to be observed with a pair of fiber-fed double spectrographs.

Our parent sample is the latest compilation of the spectroscopic quasar catalog (Schneider et al. 2010) from SDSS DR7 (Abazajian et al. 2009). This sample contains 105,783

bona fide quasars brighter than $M_i = -22.0$ and have at least one broad emission line with FWHM larger than 1000 km s^{-1} or have interesting/complex absorption features. About half of these objects are selected uniformly using the final quasar target selection algorithm described in Richards et al. (2002a), with the remaining objects selected via early versions of the target selection algorithm or various serendipitous algorithms (see Schneider et al. 2010), whose selection completeness cannot be readily quantified. For statistical studies such as quasar clustering and the LF, one should use the uniformly selected quasar sample. Fig. 1 shows the distribution of the 105,783 quasars in the redshift-luminosity plane.

The reduced one-dimensional (1D) spectral data used in this study are available through the SDSS Data Archive Server[1] (DAS). The spectral resolution is $R \sim 1850 - 2200$, and the 1D spectra are stored in vacuum wavelength, with a pixel scale of 10^{-4} in log-wavelength, which corresponds to ~ 69 kms^{-1}. Since the 6th SDSS data release (DR6, Adelman-McCarthy et al. 2008), the spectral flux calibration is scaled to the point spread function (PSF) magnitudes of standard stars, therefore there is no longer need for a fiber-to-PSF conversion for the spectral flux (Shen et al. 2008 also used the PSF spectral flux calibration). Throughout the paper, we refer to the signal-to-noise ratio per pixel as S/N.

To include radio properties, we match the DR7 quasar catalog with the FIRST (White et al. 1997) catalog[2] with a matching radius of 30" and estimate the radio loudness $R = f_{6cm}/f_{2500}$ following Jiang et al. (2007), where f_{6cm} and f_{2500} are the flux density (f_ν) at rest-frame 6 cm and 2500 Å, respectively. For the quasars that have only one FIRST source within 30" we match them again to the FIRST catalog with a matching radius 5" and classify the matched ones as core-dominant radio quasars. Those quasars that have multiple FIRST source matches within 30" are classified as lobe-dominated. The rest-frame 6 cm flux density is determined from the FIRST integrated flux density at 20 cm assuming a power-law slope of $\alpha_\nu = -0.5$; the rest-frame 2500 Å flux density is determined from the power-law continuum fit to the spectrum as described in §3. For lobe-dominated radio quasars we use all the matched FIRST sources to compute the radio flux density. We note that we may have missed some double-lobed radio quasars with lobe diameter larger than 1'.

To flag BALQSOs, we use the Gibson et al. (2009) DR5 BALQSO catalog to set the CIV and MgII BALQSO flags (using their "BI0" flags). We also visually inspected all the post-DR5 quasars with redshift $z > 1.45$ to identify obvious CIV BALQSOs (we may have missed some weak BALQSOs). We did not perform a systematic search for low-ionization

---

[1]http://das.sdss.org/spectro/

[2]The version of the FIRST source catalog and the coverage maps used are as of July 16, 2008 (http://sundog.stsci.edu/first/catalogs/readme.html).

Mg II BALQSOs because of the large number of quasars with Mg II coverage and the much rarer occurrence of Mg II BALQSOs. Although we report serendipitously identified Mg II BALQSOs, the completeness of these objects is low. We identified a total of 6214 BALQSOs in the DR7 quasar catalog.

There are also subclasses of quasars which show interesting spectral features in their broad or narrow emission line profiles. Some quasars show a double-peaked or asymmetric broad Balmer line profile, which is commonly interpreted as arising from a relativistic accretion disk around the black hole (disk emitters, e.g., Chen et al. 1989; Eracleous & Halpern 1994; Strateva et al. 2003) although alternative interpretations exist for some of these objects, such as a binary SMBH (e.g., Gaskell 2010, and references therein). Some quasars show double-peaked narrow lines (such as [O III] $\lambda\lambda$4959,5007, e.g., Liu et al. 2010a; Smith et al. 2009; Wang et al. 2009a), which could be due to either narrow line region kinematics or a merging AGN pair (e.g., Liu et al. 2010b; Shen et al. 2011). We have visually inspected all of the $z < 0.89$ quasars in the DR7 catalog (i.e., those with Hβ coverage) and flagged such objects.

3. Spectral Measurements

We are primarily interested in the broad Hα, Hβ, Mg II, and C IV emission lines because these are the most frequently studied lines that are available over a wide range of redshifts. More importantly, they have been calibrated as virial black hole (BH) mass estimators (e.g., Vestergaard 2002; McLure & Jarvis 2002; McLure & Dunlop 2004; Greene & Ho 2005b; Vestergaard & Peterson 2006; McGill et al. 2008; Vestergaard & Osmer 2009; Wang et al. 2009b).

There are numerous studies of the statistical emission line properties of quasars relying either on direct measurements, or on spectral fits of the line profile (e.g., Boroson & Green 1992; Marziani et al. 1996; McLure & Jarvis 2002; Richards et al. 2002b; McLure & Dunlop 2004; Bachev et al. 2004; Dietrich & Hamann 2004; Baskin & Laor 2005; Kollmeier et al. 2006; Fine et al. 2006, 2008; Bonning et al. 2007; Salviander et al. 2007; Sulentic et al. 2007; Shen et al. 2008a,b; Hu et al. 2008a,b; Zamfir et al. 2010; Wang et al. 2009b; Wu et al. 2009; Dong et al. 2009b,a). For the same set of data, different studies sometimes report different results for certain measured quantities due to the different line-measurement techniques used in these studies. Which method is preferred, however, depends on the nature of the problem under study. A classic example is measuring the *full-width-at-half-maximum* (FWHM) in estimating the BH mass using virial estimators, where the usual complications are: 1) how to subtract the continuum underneath the line; 2) how to treat
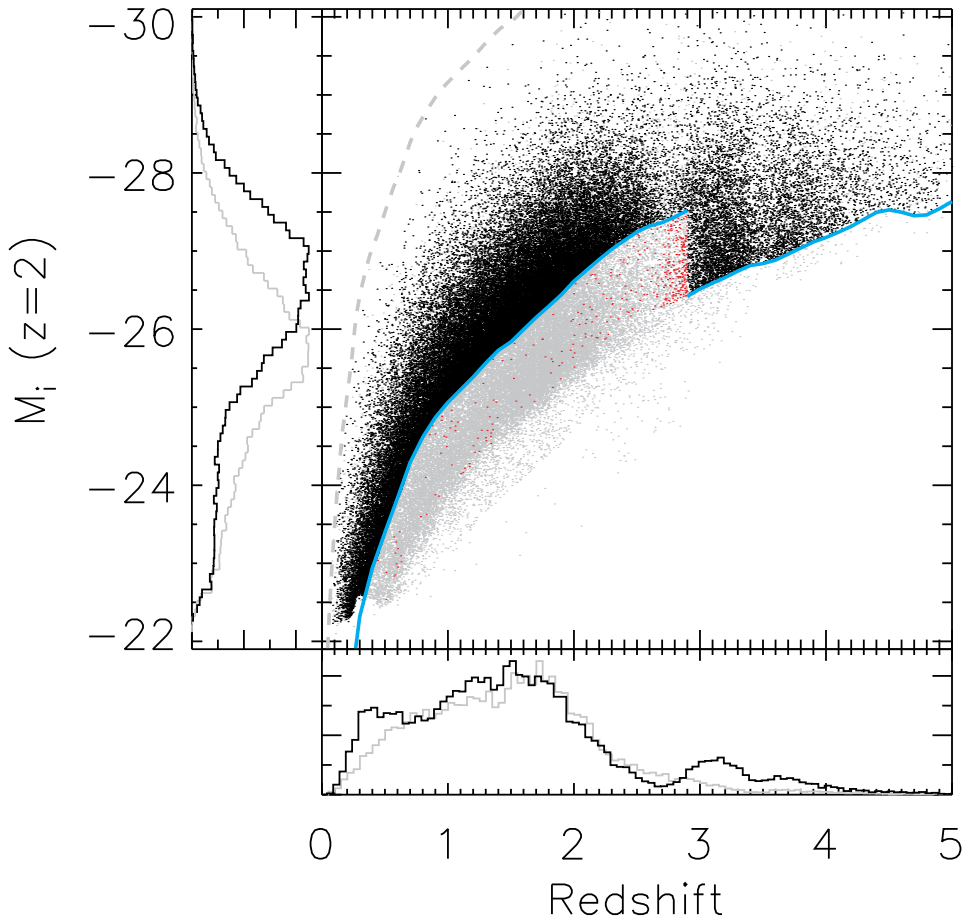
Fig. 1.— The distribution of DR7 quasars in luminosity-redshift space, where the left and bottom panels show the luminosity and redshift histograms. Luminosity is indicated using the (continuum and emission line) K-corrected, i-band absolute magnitude, $M_i(z = 2)$, normalized at $z = 2$ (Richards et al. 2006a). The black dots are uniformly-selected quasars (see Richards et al. 2002a and §3.8) and the gray dots are quasars selected by a variety of earlier algorithms or serendipitous selections. The red dots are selected by the `QSO_HiZ` uniform selection (e.g., Richards et al. 2002a) but with $i > 19.1$ and at $z < 2.9$, and should be removed in constructing homogeneous quasar samples. The cyan lines show the corresponding $M_i(z = 2)$ for $i = 19.1$ ($z < 2.9$) and $i = 20.2$ ($z > 2.9$) respectively, and the gray dashed line shows the equivalent for $i = 15$ (the bright limit for SDSS quasar targets). The non-uniformly selected quasars (gray dots) are targeted to fainter luminosities than are the uniformly selected quasars.

the narrow line component (especially for MgII and CIV); 3) how to measure the broad line profile, especially in the presence of noise and absorption. These choices crucially depend on the particular virial estimator calibrations used; in particular, one must use a similar FWHM definition as was used in the virial estimator calibration, and new methods of FWHM measurements must be re-calibrated either against reverberation mapping (RM) masses or internally between different line estimators. On the other hand, different line-measurement methods have different sensitivities to the quality of the spectra (spectral resolution and S/N), which introduce systematics when switching from high-quality to low-quality data (e.g., Denney et al. 2009). It is beyond our scope to fully settle these issues within the current study.

We remove the effects of Galactic extinction in the SDSS spectra using the Schlegel et al. (1998) map and a Milky Way extinction curve from Cardelli et al. (1989) with $R_V = 3.1$, and shift the spectra to restframe using the cataloged redshift as the systemic redshift[3]. For each line, we fit a local power-law continuum ($f_\lambda = A\lambda^{\alpha_\lambda}$) plus an iron template (Boroson & Green 1992; Vestergaard & Wilkes 2001; Salviander et al. 2007) to the wavelength range around the line that is not contaminated by the broad line emission. During the continuum+iron fitting we simultaneously fit five parameters: the normalization A and slope α_λ of the power-law continuum, and the normalization $A_{\rm Fe}$, line broadening $\sigma_{\rm Fe}$ and velocity offset $v_{\rm Fe}$ relative to the systemic redshift for the iron template fit. Because of the moderate spectral quality of SDSS spectra (median S/N$\lesssim$ 10) $\sigma_{\rm Fe}$ and $v_{\rm Fe}$ are often poorly constrained; nevertheless the iron fit gives a reasonably good estimate of the iron flux to be subtracted off. The continuum+iron fit is then subtracted from the spectrum, and the resulting line spectrum is modelled by various functions. In the case of Hα and Hβ the adjacent narrow emission lines, e.g., [OIII] $\lambda\lambda4959,5007$, [NII] $\lambda\lambda6548,6584$, [SII] $\lambda\lambda6717,6731$, are also fit simultaneously. Below we describe the detailed fitting procedures for the four broad lines.

3.1. Hα

For Hα we use the optical iron template from Boroson & Green (1992), and we fit for objects with $z \leq 0.39$. The continuum+iron fitting windows are [6000,6250] Å and [6800,7000] Å.

For Hα line fitting, we fit the wavelength range [6400,6800] Å. The narrow components of Hα, [NII] $\lambda\lambda6548,6584$, [SII] $\lambda\lambda6717,6731$ are each fit with a single Gaussian. Their velocity

---

[3]Hewett & Wild (2010) provided improved redshifts for SDSS quasars. However, this subtlety has negligible effects on our spectral fits.

offsets from the systemic redshift and line widths are constrained to be the same, and the relative flux ratio of the two [N II] components is fixed to 2.96. We impose an upper limit on the narrow line FWHM < 1200 km s^{-1} (e.g., Hao et al. 2005). The broad Hα component is modelled in two different ways: a) a single Gaussian with a FWHM > 1200 km s^{-1}; b) multiple Gaussians with up to three Gaussians, each with a FWHM > 1200 km s^{-1}. The second method yields similar results to the fits with a truncated Gaussian-Hermite function (e.g., van der Marel & Franx 1993). During the fitting, all lines are restricted to be emission lines (i.e., positive flux).

3.2. Hβ

For Hβ we use the optical iron template from Boroson & Green (1992), and we fit for objects with $z \leq 0.89$. The continuum+iron fitting windows are [4435,4700] Å and [5100,5535] Å. For the Hβ line fitting, we follow a similar procedure as Hα to fit for Hβ and [O III] $\lambda\lambda4959,5007$, where the line fitting wavelength range is [4700,5100] Å. Since the [O III] $\lambda\lambda4959,5007$ lines frequently show asymmetric blue wings (e.g., Heckman et al. 1981; Greene & Ho 2005a; Komossa et al. 2008) and sometimes even more dramatic double-peaked profiles (e.g., Liu et al. 2010a; Smith et al. 2009; Wang et al. 2009a), we model each of the narrow [O III] $\lambda\lambda4959,5007$ lines with two Gaussians, one for the core and the other for the blue wing. The flux ratio of the [O III] doublet is not fixed during the fit, but we found that the fitting results show good agreement with the theoretical ratio of about 3. The velocity offset and FWHM of the narrow Hβ line are tied to those of the core [O III] $\lambda\lambda4959,5007$ components[4], and we impose an upper limit of 1200 km s^{-1} on the narrow line FWHM. As in the Hα case, the broad Hβ component is modelled in two ways: either by a single Gaussian, or by multiple Gaussians with up to three Gaussians, each with a FWHM > 1200 km s^{-1}.

The single Gaussian fit to the broad component is essentially the same to the procedure in Shen et al. (2008b), and is somewhat similar to the procedure in McLure & Dunlop (2004)[5]. However, in many objects the broad Hα/Hβ component cannot be fit perfectly with a single Gaussian; and FWHMs from the single Gaussian fits are systematically larger by ~ 0.1 dex than those from the multiple Gaussian fits (e.g., Shen et al. 2008b). The

---

[4]In some objects the narrow Hβ component might have different width and velocity offset from those of the core [O III] $\lambda\lambda4959,5007$ components. Nevertheless, in such cases our procedure still provides a reasonable approximation to subtract the narrow Hβ component. Fitting the narrow Hβ line without this constraint would significantly degrade the reliability of narrow line subtraction.

[5]In addition to Gaussian profiles, McLure & Dunlop (2004) also tried to fit the broad/narrow component with a single Lorentzian, but this does not change the measured broad FWHM significantly.

additional multiple Gaussian fits for the broad Hα/Hβ component provide a better fit to the overall broad line profile, and the FWHM measured from the model flux can be used in customized virial calibrations. It is unclear, however, which FWHM is a better surrogate for the true virial velocity, that is, the one that yields the smallest scatter in the calibration against RM black hole masses.

3.3. Mg II

For Mg II we use the UV iron template from Vestergaard & Wilkes (2001), and we fit for objects with $0.35 \leq z \leq 2.25$. The continuum+iron fitting windows are [2200,2700] Å and [2900,3090] Å. We then subtract the pseudo-continuum from the spectrum, and fit for the Mg II line over the [2700,2900] Å wavelength range, with a single Gaussian (with FWHM < 1200 kms^{-1}) for the narrow Mg II component, and for the broad Mg II component with: 1) a single Gaussian; 2) multiple Gaussians with up to three Gaussians. Again, the multiple-Gaussian fits often provide a better fit to the overall broad Mg II profile; but we have retained the FWHMs from a single Gaussian fit in order to use the Mg II virial mass calibrations in McLure & Jarvis (2002) and McLure & Dunlop (2004). Some Mg II virial estimator calibrations (e.g., McLure & Jarvis 2002; McLure & Dunlop 2004; Wang et al. 2009b) do subtract a narrow Mg II component while others (e.g., Vestergaard & Osmer 2009) do not. To utilize the Mg II calibration in Vestergaard & Osmer (2009), we also measure the FWHMs from the broad+narrow Mg II fits (with multiple Gaussians for the broad component), where any Gaussian component having flux less than 5% of the total line flux is rejected when computing the FWHM — this step is to eliminate artificial noise spikes which can bias the FWHM measurements. During our fitting, we mask out 3σ outliers below the 20-pixel boxcar-smoothed spectrum to reduce the effects of narrow absorption troughs.

Unlike the cases of Hα and Hβ, it is somewhat ambiguous whether it is necessary to subtract a narrow line component for Mg II and if so, how to do it. On one hand, for some objects, such as SDSSJ002209.95+001629.3 and SDSSJ130101.94+130227.1 (e.g., Fig. 2), the spectral quality is sufficient to see the bifurcation of the Mg II doublet around the peak. The locations of the two peaks indicate that they are associated with the Mg II $\lambda\lambda$2796,2803 doublet, and the fact that they are resolved means that the FWHM of each component is $\lesssim 750$ km s^{-1}, hence they are most likely associated with the narrow line region. On the other hand, such cases are rare and most SDSS spectra do not have adequate S/N to unambiguously locate the narrow Mg II doublet. Associated narrow Mg II absorption troughs can further complicate the situation by mimicking two peaks. Hence although our approach of fitting a single Gaussian to the narrow Mg II component is not perfect, it nevertheless accounts

for some narrow $MgII$ contamination. Fig. 3 compares our broad $MgII$ FWHM measurements with those from Wang et al. (2009b) for the objects in both studies. Although we have used a different approach, our results are consistent with theirs, with a mean offset ~ 0.05 dex. This systematic offset between our results and theirs is caused by the fact that they are treating the broad $MgII$ line as a doublet as well, while we (and most studies) are treating the broad $MgII$ line as a single component.

3.4. CIV

For CIV we fit for objects with $1.5 \leq z \leq 4.95$. Iron emission is generally weak for CIV, and most of our objects do not have the spectral quality sufficient for a reliable iron template subtraction (e.g., Shen et al. 2008b). The power-law continuum fitting windows are: [1445,1465] Å and [1700,1705] Å. We found fitting CIV with iron subtraction does not change the fitted CIV FWHM significantly, but does systematically reduce the CIV EW by ~ 0.05 dex because the iron flux under the wings of the CIV line is accounted for. At the same time, fitting iron emission increases the uncertainty in the fitted continuum slope and normalization, due to imperfect subtraction of the iron flux. Therefore we report our CIV measurements without the iron template fits, and emphasize that the CIV EWs may be overestimated by ~ 0.05 dex on average.

The continuum subtracted line emission within [1500,1600] Å was fitted with three Gaussians (e.g., Shen et al. 2008b), and we measure the line FWHM from the model fit. To reduce the effects of noise spikes, we reject any Gaussian component having flux less than 5% of the total model flux when computing the FWHM. However, unlike some attempts in the literature (e.g., Bachev et al. 2004; Baskin & Laor 2005; Sulentic et al. 2007; Zamfir et al. 2010), we do not subtract a narrow CIV component because: 1) it is still debatable if a strong narrow CIV component exists for most quasars, or if it is feasible to do such a subtraction; 2) existing CIV virial estimators are calibrated using the FWHMs from the entire CIV profile (Vestergaard & Peterson 2006).

Many CIV lines are affected by narrow or broad absorption features. To reduce the effects of such absorption on the CIV fits, we mask out 3σ outliers below the 20-pixel boxcar-smoothed spectrum during our fits (to remedy for narrow absorption features); we also perform a second fit excluding pixels below 3σ of the first model fit, and replace the first one if statistically justified (to account for broad absorption features). We found these recipes can alleviate the impact of narrow or moderate absorption features, but the improvement is marginal for objects severely affected by broad absorption.
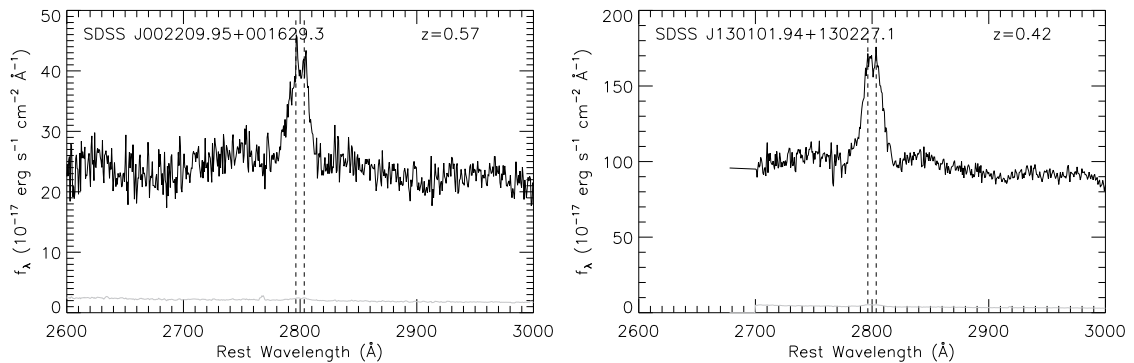
Fig. 2.— Two examples of Mg II lines which show narrow line components. The spectra are plotted as black lines and the gray lines show the errors per pixel. The dashed vertical lines mark the locations of the Mg II $\lambda\lambda2796,2803$ doublet.
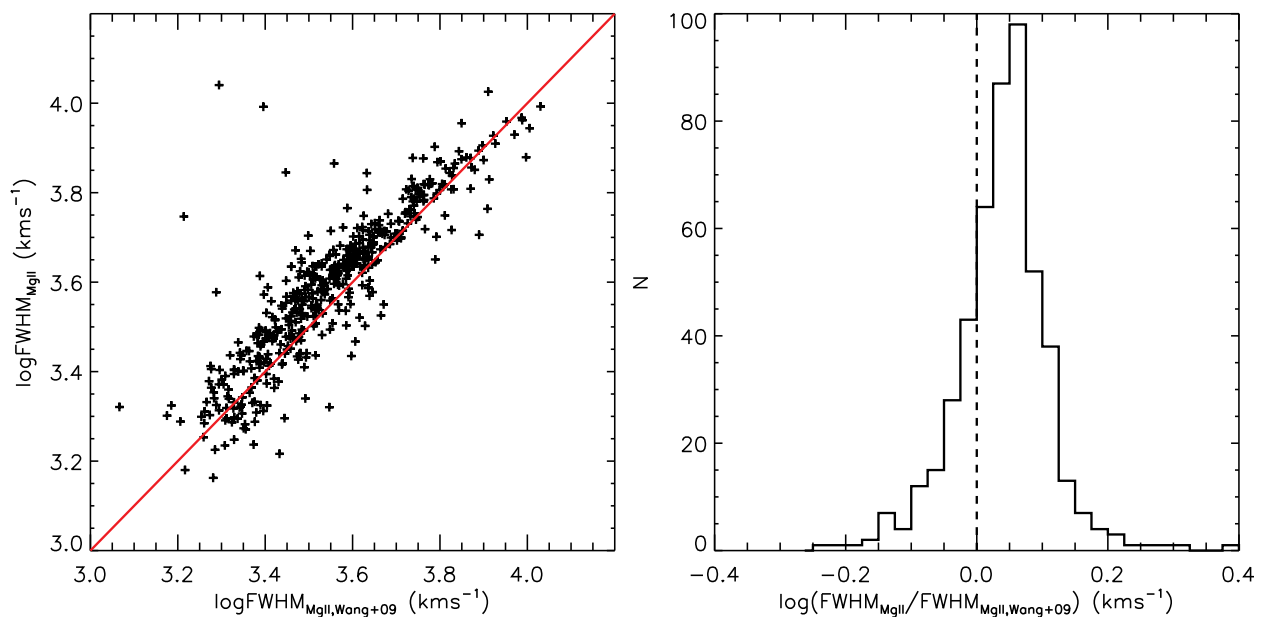

Fig. 3.— Comparison of our Mg II FWHMs with those from Wang et al. (2009b) for the same objects. The left panel shows a scatter plot, where the solid line is the unity relation. The right panel shows a histogram of the ratio between the two values. Our broad Mg II FWHM values are systematically larger by ~ 0.05 dex than those in Wang et al. (2009b), mainly caused by the fact that they fit the broad Mg II as a doublet while we did not.
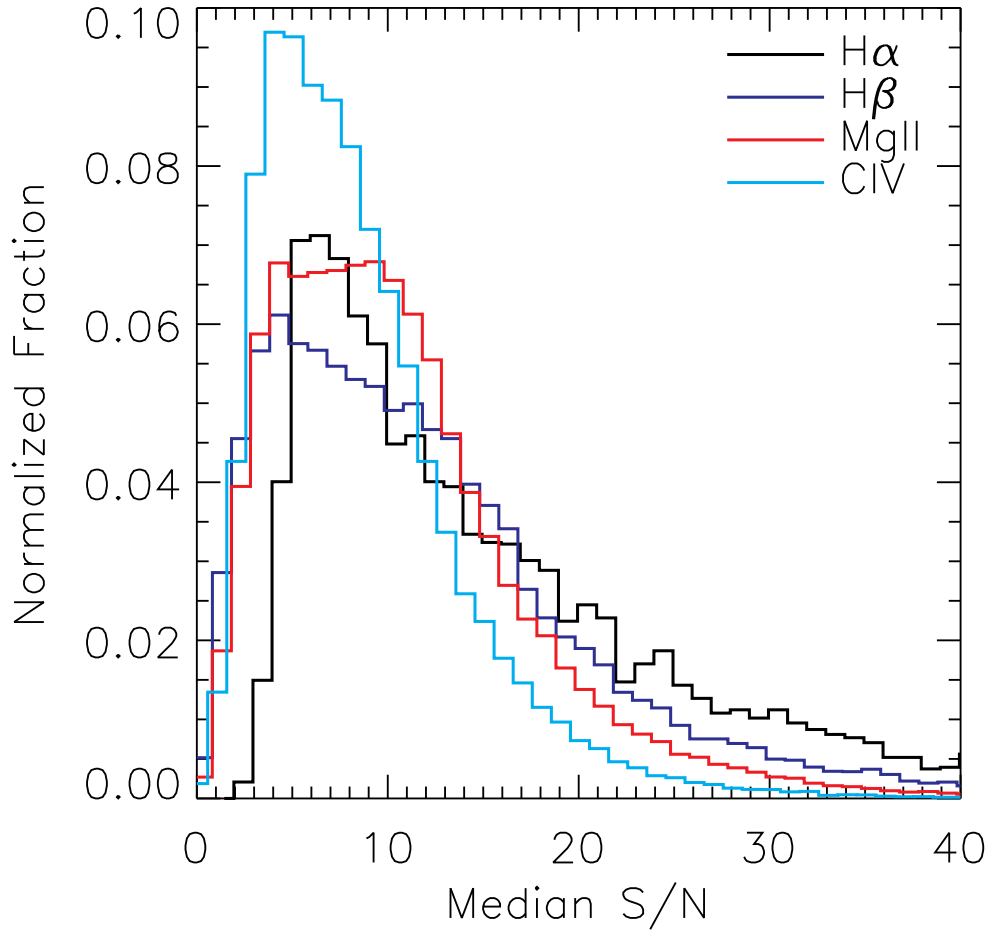
Fig. 4.— Distributions of the median S/N per pixel around the line-fitting regions for objects with line measurements, for Hα, Hβ, MgII and CIV respectively, where the underlying area of each distribution is normalized at unity.

3.5. Reliability of spectral fits and error estimation

Our spectral fits were performed in an automatic fashion. Upon visual inspection of the fitting results we are confident that the vast majority of the fits to high S/N spectra were successful, and comparisons with independent fits by others also show good agreement. However, the reliability of our spectral fits drops rapidly for low-quality spectra. Fig. 4 shows the distributions of the median S/N per pixel around the line-fitting region for objects that have line measurements, for Hα, Hβ, Mg$_{II}$ and C$_{IV}$ respectively. Although the bulk of objects have median S/N> 5 for the line-fitting regions, there are many objects that have lower median S/N, especially for C$_{IV}$ at high redshift. The effects of S/N on the measurements depend on both the properties of the lines (i.e., line profile, line strength, degree of absorption features, etc), and the line-fitting technique itself (i.e., what functional form was used, how to deal with absorption troughs, etc).

To investigate the impact of S/N on our fitting parameters we ran a series of Monte Carlo simulations. We select representative real spectra with high S/N, then degrade the spectra by adding Gaussian noise and measure the line properties using the same line-fitting routine. For each line (Hβ, Mg$_{II}$, or C$_{IV}$), we study several objects with various line shapes and EWs. We simulate 500 trials for each S/N level and take the median and the 68% range as the measurement result and its error.

Figs. 5-8 show several examples of our investigations for Hα, Hβ, Mg$_{II}$ and C$_{IV}$ respectively. As expected, decreasing the S/N increases measurement scatter. In all cases the fitted continuum is unbiased as S/N decreases. The FWHMs and EWs are biased by less than $\pm 20\%$ for high-EW objects as S/N is reduced to as low as ~ 3. For low-EW objects, the FWHMs and EWs are biased low/high by $> 20\%$ for S/N$\lesssim 5$. Since the median EWs for the three lines are > 30 Å (see Figs. 12-14), we expect that the measurements for most objects are unbiased to within $\pm 20\%$ down to S/N~ 3. But for many purposes, it would be more conservative to impose a cut at S/N> 5 for reliable measurements.

To estimate the uncertainties in the measured quantities in our fits, we generate 50 mock spectra by adding Gaussian noise to the original spectrum using the reported flux density errors, and fit for those mock spectra with the same fitting routines. We estimate the measurement uncertainties from the 68% range (centered on the median) of the distributions of fitting results of the 50 trials. This approach gives more reasonable error estimation than using the statistical errors resulting from the χ^2 fits, in the sense that it not only takes into account the spectral S/N but also the ambiguity of subtracting a narrow line component in many cases (for Hα, Hβ and Mg$_{II}$). We estimate the spectral measurement uncertainties for all the 105,783 quasars in our sample in this way.
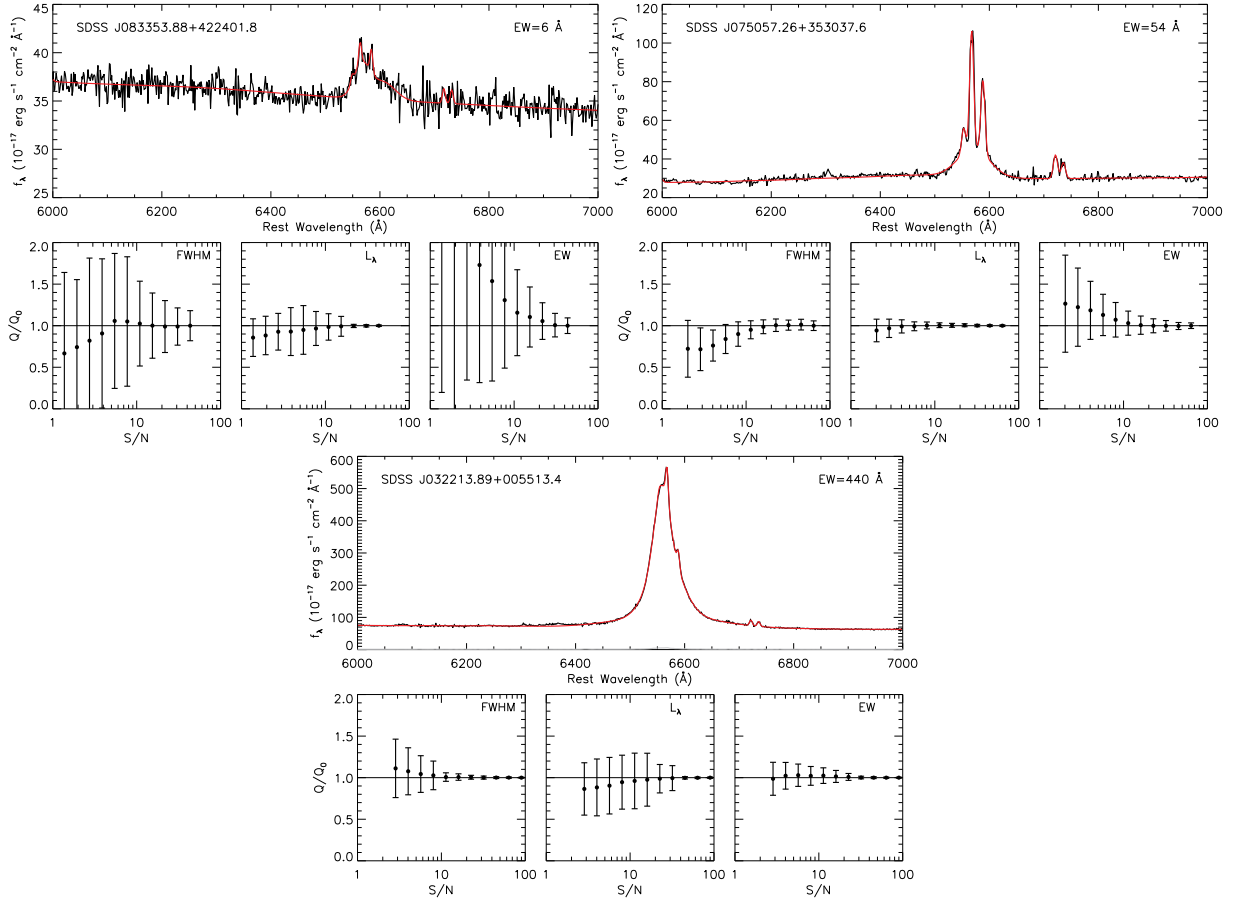
Fig. 5.— Effects of S/N on the line measurements for Hα for three representative examples. For each object we show the actual spectrum (black line) and the best-fit model (red line) in the upper panel. The lower three panels show the ratios of the values measured from the degraded spectra to those measured from the original spectrum, as functions of S/N; black dots are median values and the error bars indicate the 68% quantile.

Fig. 6.— Effects of S/N on the line measurements for Hβ for three representative examples. For each object we show the actual spectrum (black line) and the best-fit model (red line) in the upper panel. The lower three panels show the ratios of the values measured from the degraded spectra to those measured from the original spectrum, as functions of S/N; black dots are median values and the error bars indicate the 68% quantile.
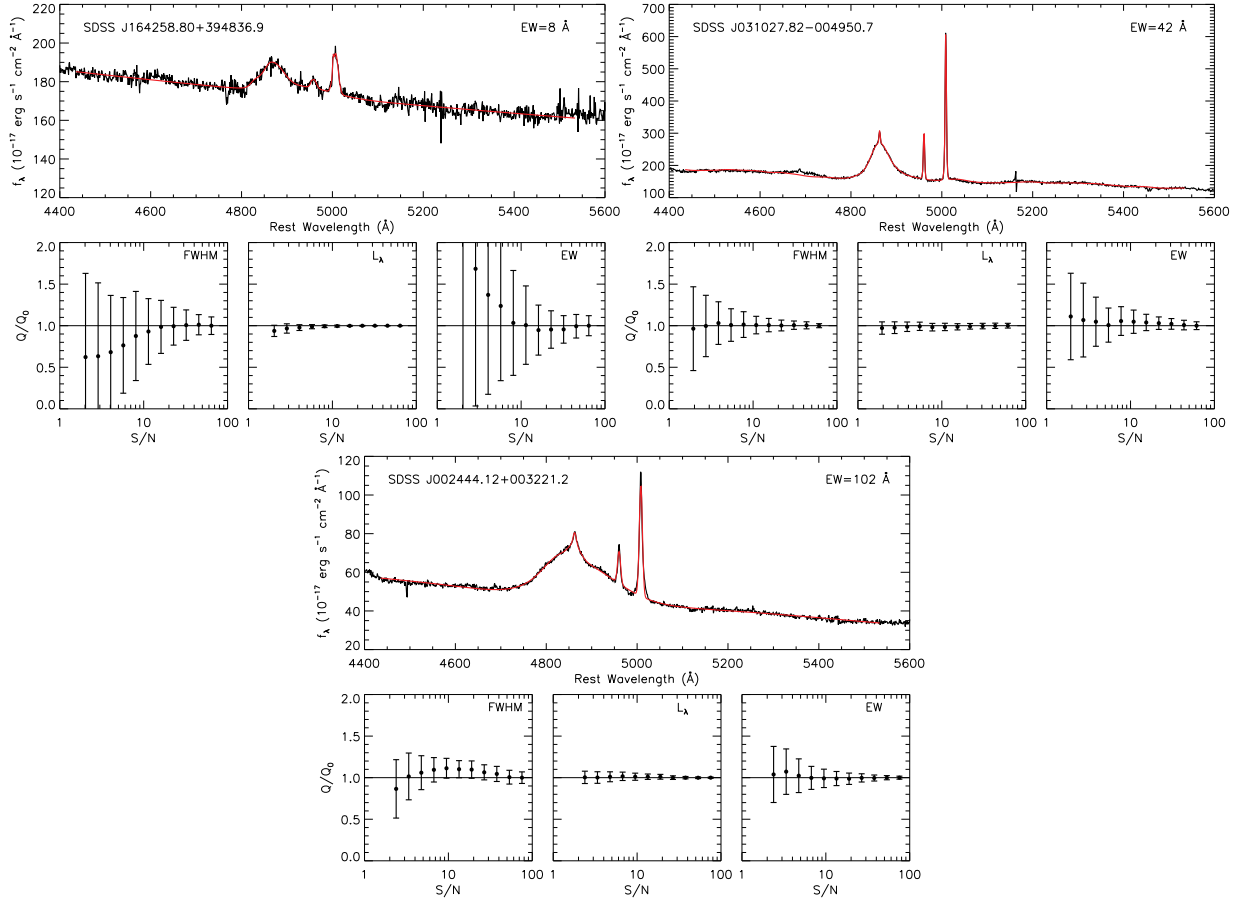
Fig. 7.— Effects of S/N on the line measurements for Mgɪɪ for three representative examples. For each object we show the actual spectrum (black line) and the best-fit model (red line) in the upper panel. The lower three panels show the ratios of the values measured from the degraded spectra to those measured from the original spectrum, as functions of S/N; black dots are median values and the e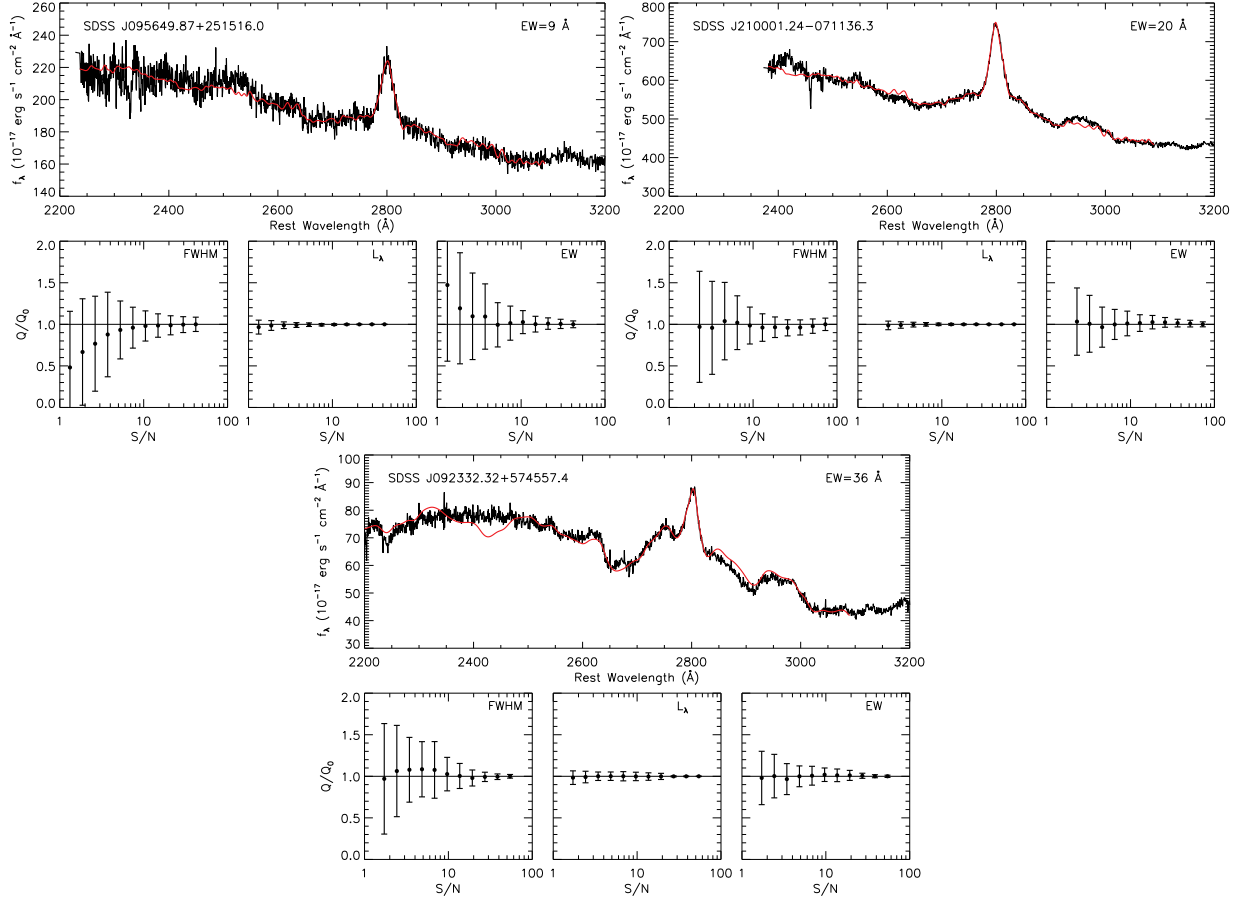rror bars indicate the 68% quantile. Note that our continuum+iron fit does not account for the [Ne ɪᴠ]/Fe ɪɪɪ and [O ɪɪ] emission around 2400 Å-2480 Å.
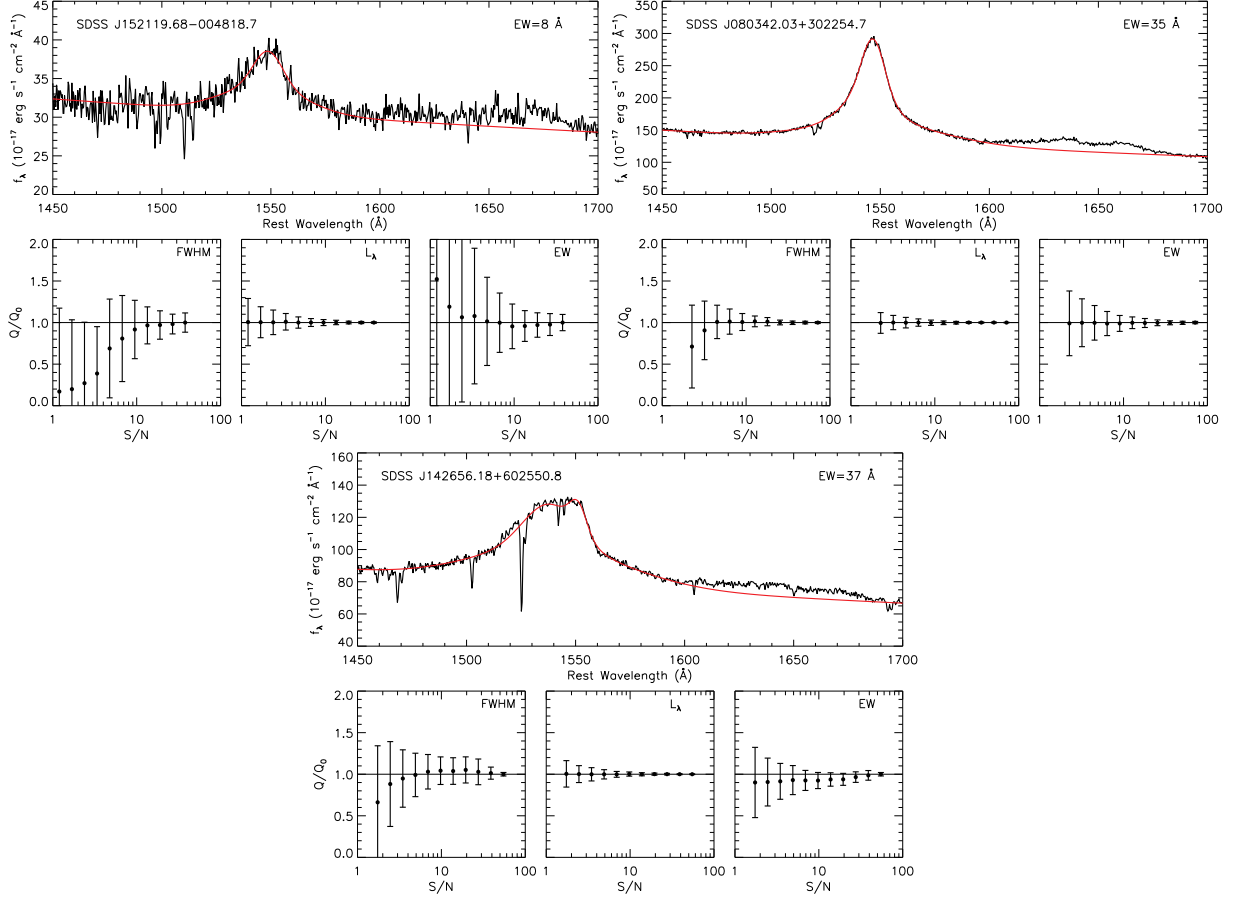
Fig. 8.— Effects of S/N on the line measurements for C IV for three representative examples. For each object we show the actual spectrum (black line) and the best-fit model (red line) in the upper panel. The lower three panels show the ratios of the values measured from the degraded spectra to those measured from the original spectrum, as functions of S/N; black dots are median values and the error bars indicate the 68% quantile. Note that the He II/O III] complex around 1650Å is not fitted.
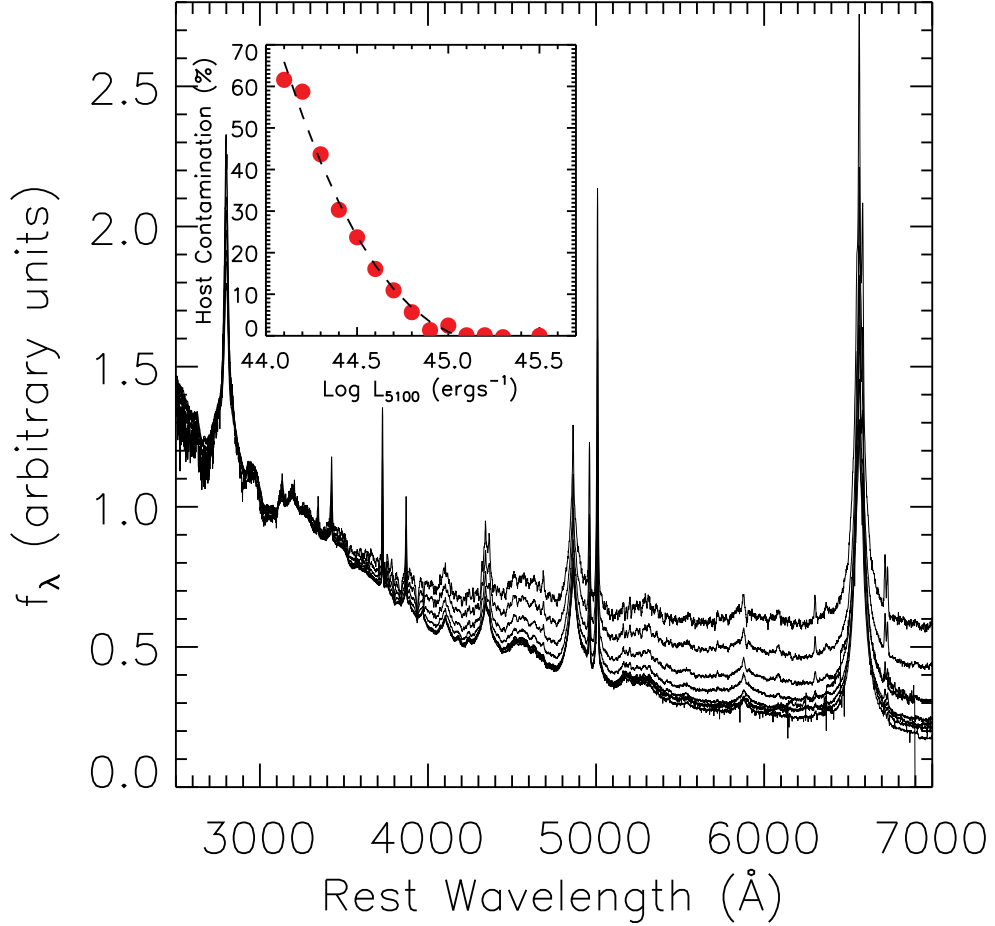
Fig. 9.— Composite spectra for objects binned in $\log L_{5100}$, normalized at 3000Å. The flux gradually flattens at long wavelength due to increasing host contamination towards fainter quasar luminosities, accompanied by the increasing prominence of stellar absorption features and narrow line emission. The inset shows the fractional host contamination at 5100Å assuming that the highest luminosity bin ($\log L_{5100} = 45.5$) is not affected by host emission and that the intrinsic AGN power-law continuum slope does not change over the luminosity range considered. The dashed line in the inset is a polynomial fit (Eqn. 1).

Finally we note that our automatic fitting procedure was optimized for the vast majority of quasars in our sample, and it may fail badly for rare objects with peculiar continuum and emission line properties (severe BALQSOs, disk emitters, etc.), such as J094215.12+090015.8 which has extremely broad lines.

3.6. Host galaxy contamination

For the vast majority of objects in our catalog with $z \gtrsim 0.5$, host galaxy contamination is negligible. However, for the $z \lesssim 0.5$ low-luminosity quasars in our sample, the continuum luminosity at restframe 5100Å may be contaminated by light from the host galaxies. Unfortunately the spectral quality of the majority of individual objects does not allow a reliable galaxy continuum subtraction. Here we estimate the effects of host contamination with stacked spectra.

We take all quasars with measurable rest frame 5100Å continuum luminosity, L_{5100}, and bin them on a grid of $\Delta \log L_{5100} = 0.1$ for $\log(L_{5100}/\mathrm{erg\,s^{-1}}) = 44.1 - 45.5$. Following Vanden Berk et al. (2001), we generate geometric mean composite spectra for objects in each luminosity bin. The composite spectra are shown in Fig. 9, where the flux gradually flattens at long wavelengths due to increasing host contamination at fainter luminosities. This trend is accompanied by the increasing prominence of stellar absorption features and narrow line emission towards fainter luminosities. The inset shows the fractional host contamination at 5100Å assuming that the highest luminosity bin ($\log L_{5100} = 45.5$) is not affected by the host and that the intrinsic AGN power-law continuum slope does not change over the luminosity range considered. The host contamination is substantial at $\log L_{5100} < 44.5$, and becomes negligible towards higher luminosities. The median value of $\log L_{5100}$ for quasars in this low-redshift sample is ~ 44.6, and therefore the host contamination on average is $\sim 15\%$, which leads to a ~ 0.06 dex overestimation of the 5100Å continuum luminosity and thus ~ 0.03 dex overestimation of the Hβ-based virial masses for the median object. While we do not correct the measured 5100Å continuum luminosity (and other quantities depending on it) in the catalog, we provide an empirical fitting formula of the average host contamination based on the stacked spectra (dashed line in the inset of Fig. 9):

$$\frac{L_{5100,\mathrm{host}}}{L_{5100,\mathrm{QSO}}} = 0.8052 - 1.5502x + 0.9121x^2 - 0.1577x^3 \tag{1}$$

for $x + 44 \equiv \log(L_{5100,\mathrm{total}}/\mathrm{erg\,s^{-1}}) < 45.053$; no correction is needed for luminosities above this value.

We suspect that host contamination is largely responsible for the apparent anti-correlation

between L_{5100} and spectral slope α_λ, and the "negative" Baldwin effect (e.g., Baldwin 1977) between the broad Hβ EW and L_{5100} below $L_{5100} \sim 10^{45}$ ergs^{-1} (see §4.1).

3.7. Virial BH masses

It has become common practice to estimate quasar/AGN BH masses based on single-epoch spectra (hereafter virial mass in short). This approach assumes that the broad line region (BLR) is virialized, the continuum luminosity[6] is used as a proxy for the BLR radius, and the broad line width (FWHM or line dispersion) is used as a proxy for the virial velocity. The virial mass estimate can be expressed as:

$$\log\left(\frac{M_{\rm BH,vir}}{M_\odot}\right) = a + b\log\left(\frac{\lambda L_\lambda}{10^{44}\,{\rm erg\,s^{-1}}}\right) + 2\log\left(\frac{\rm FWHM}{\rm km\,s^{-1}}\right)\ , \tag{2}$$

where the coefficients a and b are empirically calibrated against local AGNs with RM masses or internally among different lines. Hβ, Mg$_{\rm II}$, C$_{\rm IV}$, and their corresponding continuum luminosities are all frequently adopted in such virial calibrations. Although it is straightforward to calibrate and use these virial estimators, one must bear in mind the large uncertainties ($\gtrsim 0.4$ dex) associated with these estimates and the systematics involved in the calibration and usage, which will potentially lead to significant biases of these BH mass estimates (e.g., Collin et al. 2006; Shen et al. 2008b; Marconi et al. 2008; Denney et al. 2009; Kelly et al. 2009; Shen & Kelly 2010).

The virial BH mass calibrations used in this paper are from McLure & Dunlop (2004, Hβ and Mg$_{\rm II}$), Vestergaard & Peterson (2006, Hβ and C$_{\rm IV}$), and Vestergaard & Osmer (2009, Mg$_{\rm II}$). These calibrations have parameters:

$$(a, b) = (0.672, 0.61), \qquad {\rm MD04;\ H}\beta \tag{3}$$
$$(a, b) = (0.505, 0.62), \qquad {\rm MD04;\ Mg_{II}} \tag{4}$$
$$(a, b) = (0.910, 0.50), \qquad {\rm VP06;\ H}\beta \tag{5}$$
$$(a, b) = (0.660, 0.53), \qquad {\rm VP06;\ C_{IV}} \tag{6}$$
$$(a, b) = (0.860, 0.50), \qquad {\rm VO09;\ Mg_{II}} \tag{7}$$

In using each of these relations we choose the proper FWHM definition adopted in these calibrations. In order to utilize our new Mg$_{\rm II}$ FWHM measurements (e.g., multiple-Gaussian

---

[6]We note that in a few extremely radio-loud quasars, the continuum luminosity is significantly boosted by the optical emission from the jet, which will then lead to overestimation of the BLR size and the virial BH mass (e.g., Wu et al. 2004). The fraction of such objects in our sample is tiny and hence we neglect this detail. But we caution the usage of cataloged virial BH masses for such objects.

fits with narrow line subtraction, see §3.3), we adopt the $b = 0.62$ slope in the BLR radius−luminosity relation in McLure & Dunlop (2004), and recalibrate the coefficient a such that the MgII-based estimates are consistent with the Hβ-based (VP06) estimates on average. We choose this particular slope b because it was re-calibrated in McLure & Dunlop (2004) using a subsample of reverberation mapping AGNs that occupy the high-luminosity regime in the local RM AGN sample, arguably better than using the whole RM sample. We choose the VP06 Hβ formula to calibrate our MgII formula because the FWHMs of broad Hβ and MgII were measured in a similar fashion (as opposed to the single-Gaussian or Lorentzian profile adopted in McLure & Dunlop 2004). This new MgII calibration is

$$(a, b) = (0.740, 0.62), \qquad \text{S10; Mg\textsc{ii} .} \tag{8}$$

In some cases a particular line may be unavailable in the spectrum, or the continuum is too faint to measure. Below we provide several alternative empirical recipes to estimate a virial BH mass. These recipes are calibrated using correlations among continuum and emission line properties, and are *only* valid in the average sense. We recommend to use them only when the above estimators are unavailable.

Following Greene & Ho (2005b), a virial BH mass can be estimated based on the FWHM and luminosity of the broad Hα line. We found a correlation between the FWHMs (using multiple-Gaussian fits) of the broad Hα and Hβ lines similar to that found in previous work (e.g., Greene & Ho 2005b; Shen et al. 2008a), with the broad Hβ FWHM systematically larger than the broad Hα FWHM:

$$\log\left(\frac{\text{FWHM}_{\text{H}\beta}}{\text{km\,s}^{-1}}\right) = (-0.11 \pm 0.03) + (1.05 \pm 0.01)\log\left(\frac{\text{FWHM}_{\text{H}\alpha}}{\text{km\,s}^{-1}}\right) \tag{9}$$

where the slope and intercept are determined using the BCES bisector linear regression estimator (e.g., Akritas & Bershady 1996) for a sample of ~ 2400 quasars with both Hα and Hβ FWHM measurements and FWHM errors less than $500\,\text{km s}^{-1}$. Our continuum luminosities at 5100 Å have a narrow dynamical range and suffer from host contamination at the low-luminosity end, hence instead of fitting a new relation using our measurements, we adopt the relation between 5100 Å continuum luminosity and Hα line luminosity in Greene & Ho (2005b, their eqn. 1). The virial mass estimator based on Hα therefore reads

$$\log\left(\frac{M_{\text{BH,vir}}}{M_\odot}\right)_{\text{H}\alpha} = 0.379 + 0.43\log\left(\frac{L_{\text{H}\alpha}}{10^{42}\,\text{erg\,s}^{-1}}\right) + 2.1\log\left(\frac{\text{FWHM}_{\text{H}\alpha}}{\text{km\,s}^{-1}}\right) , \tag{10}$$

where $L_{\text{H}\alpha}$ is the total Hα line luminosity. For quasars in our sample, Eqn. (10) yields virial BH masses consistent with the VP06 Hβ results, with a mean offset ~ 0.08 dex and a dispersion ~ 0.18 dex.

Similarly, we can substitute the continuum luminosity in the above recipes for Hβ, MgII and CIV with the luminosity of the particular line used, given that for broad line quasars the line luminosity correlates with the continuum luminosity to some extent. We determine these correlations using subsamples of quasars for which both luminosities were measured with an uncertainty < 0.03 dex. For the same reason as Hα, we do not fit a new relation between the Hβ line luminosity and continuum luminosity at $5100\,\text{Å}$, and we refer to eqn. (2) of Greene & Ho (2005b) for such a relation. The following relations are determined again using the BCES linear regression estimator (for both the bisector fit and the $Y|X$ fit, where the latter refers to "predict Y as a function of X"), where the line luminosity refers to the total line luminosity[7]:

$$\log\left(\frac{L_{\text{MgII}}}{\text{erg s}^{-1}}\right) = (2.22 \pm 0.09) + (0.909 \pm 0.002)\log\left(\frac{L_{3000}}{\text{erg s}^{-1}}\right), \quad \text{bisector}, \quad (11)$$

$$\log\left(\frac{L_{3000}}{\text{erg s}^{-1}}\right) = (1.22 \pm 0.11) + (1.016 \pm 0.003)\log\left(\frac{L_{\text{MgII}}}{\text{erg s}^{-1}}\right), \quad (\text{Y}|\text{X}), \quad (12)$$

where the scatter of this correlation is ~ 0.15 (0.16) dex for $\sim 44,000$ quasars, and

$$\log\left(\frac{L_{\text{CIV}}}{\text{erg s}^{-1}}\right) = (4.42 \pm 0.27) + (0.872 \pm 0.006)\log\left(\frac{L_{1350}}{\text{erg s}^{-1}}\right), \quad \text{bisector}, \quad (13)$$

$$\log\left(\frac{L_{1350}}{\text{erg s}^{-1}}\right) = (7.66 \pm 0.41) + (0.863 \pm 0.009)\log\left(\frac{L_{\text{CIV}}}{\text{erg s}^{-1}}\right), \quad (\text{Y}|\text{X}), \quad (14)$$

where the scatter of this correlation is ~ 0.18 (0.2) dex for $\sim 10,000$ quasars. Using our measurements, one can also estimate these correlations with other linear regression algorithms. If we substitute $\log L_{3000}$ and $\log L_{1350}$ using Eqns. (12) and (14) in the MgII and CIV estimators, we obtain virial BH masses consistent with the original recipes with no mean offset (< 0.02 dex) and negligible scatter (~ 0.1 dex).

There are systematic differences among different versions of virial calibrations. For instance, the calibrations for Hβ and MgII in McLure & Dunlop (2004) used the old RM masses and virial coefficient, while those in Vestergaard & Peterson (2006) and Vestergaard & Osmer (2009) used the updated RM masses and virial coefficient (Onken et al. 2004). Significant uncertainties of the virial coefficient still remain (e.g., Woo et al. 2010; Graham et al. 2011). Moreover, different versions of virial calibration for the same line have different dependence on luminosity, and they usually measure the line FWHM differently (even though

---

[7]For MgII, the difference between the total line luminosity and the broad line luminosity is small enough such that it essentially makes no difference in the linear regression results when we use the broad line luminosity instead.
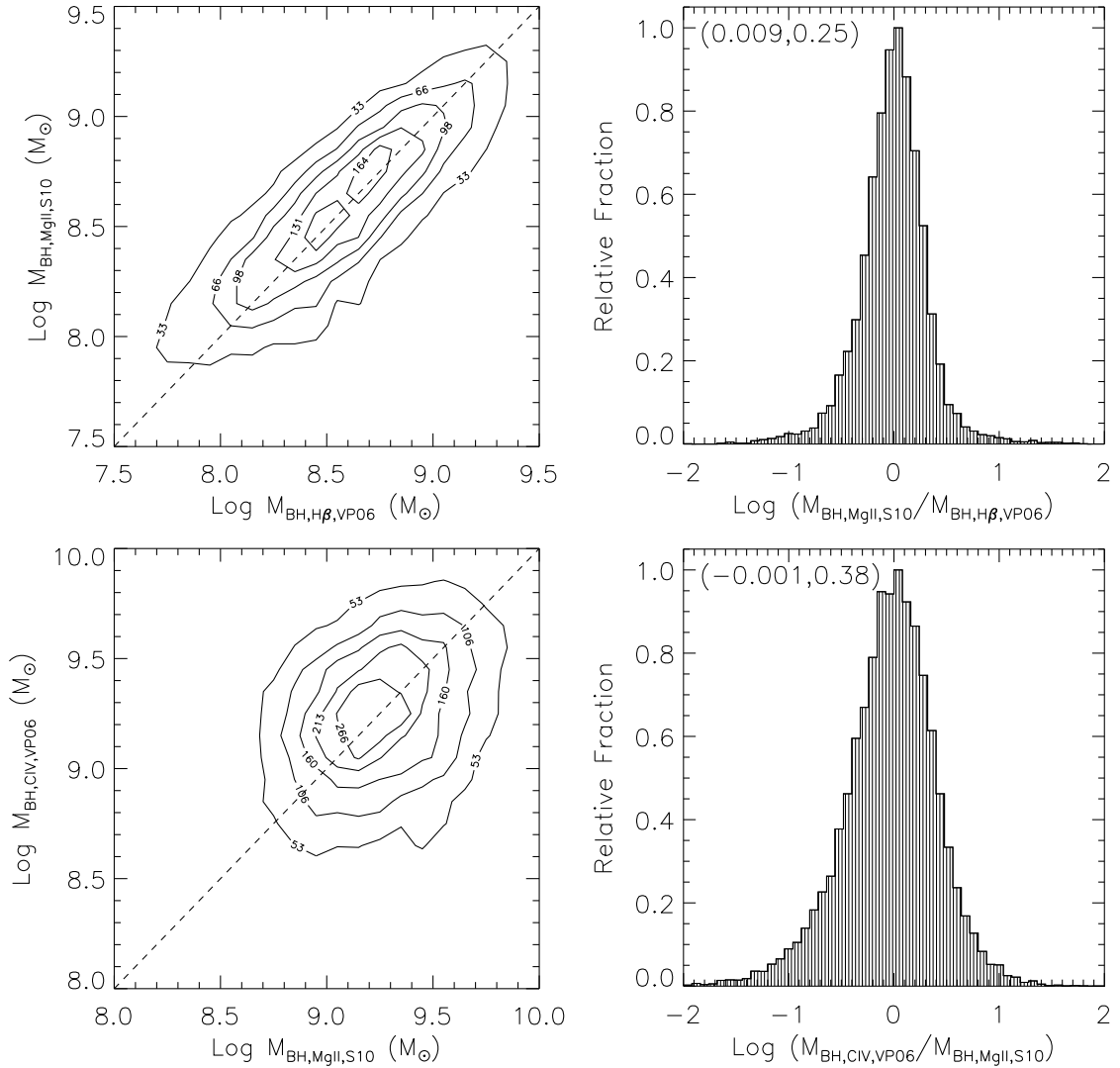
Fig. 10.— Comparison of virial masses between two different line estimators for the subset of quasars in our sample for which both line estimates are available and the median line S/N per pixel > 6. The left panels are one-to-one plots, where the contours are local point density contours estimated with a grid size of $\Delta = 0.1$ on both axes. The right panels show the distribution of mass ratios between two lines, and the mean and 1σ from a Gaussian fit to the distribution are indicated in the top-left corner. Our new Mg<small>II</small> recipe gives consistent virial mass estimates as the VP06 Hβ recipe (by design), and it also yields consistent virial mass estimates as C<small>IV</small> (VP06). These comparison results are similar to those in Shen et al. (2008b, fig. 6), where we compared between Hβ (MD04), Mg<small>II</small> (MD04) and C<small>IV</small> (VP06).

occasionally different approaches to measure the FWHM yield the same value during the multi-parameter fits), or prefer an alternative proxy (e.g., line dispersion) for the virial velocity (e.g., Collin et al. 2006; Rafiee & Hall 2010). Currently there is no consensus on which version of calibration is better. It is important to explore various systematics with RM AGN samples and statistical quasar samples to determine which is the best approach to estimate quasar BH masses with the virial technique, and this is work in progress (e.g., Onken & Kollmeier 2008; Denney et al. 2009; Wang et al. 2009b; Rafiee & Hall 2010). In the mean time, there is strong need to increase the sample size and representativity of AGNs with RM measurements, which anchor these single-epoch virial estimators.

Here we simply settle on a fiducial virial mass estimate: we use Hβ (VP06) estimates for $z < 0.7$, Mg II (S10) estimates for $0.7 \leq z < 1.9$ and C IV (VP06) estimates for $z \geq 1.9$. Fig. 10 shows the comparison between these virial estimates between two lines for the subset of quasars for which both line estimates are available and the median line S/N> 6. There is negligible mean offset (< 0.01 dex) between these virial estimates, which motivated our choice of these three calibrations. However, as noted in Shen et al. (2008b), there is a strong trend of decreasing the ratio of $\log(M_{\rm BH}^{\rm MgII}/M_{\rm BH}^{\rm CIV})$ with increasing C IV-Mg II blueshifts, indicating a possible non-virialized component in C IV. Richards et al. (2011) further developed a unified picture in which the C IV line has both a non-virial wind component and a traditional virial component, and it is plausible that the BH mass scaling relation based on C IV is only relevant for objects dominated by the virial component.

3.8. The spectral catalog

We have tabulated all the measured quantities from the spectral fitting in the online catalog of this paper, along with other properties[8]. The current compilation extends our earlier SDSS Data Release 5 (DR5) compilation (Shen et al. 2008b) by including the post-DR5 quasars, as well as measurements based on new multiple-Gaussian fits to the lines (as discussed above). The format of the catalog is described in Table 1. Objects are in the same order as the DR7 quasar catalog in Schneider et al. (2010). Below we describe the specifics of the cataloged quantities. The SDSS terminology can be found on the SDSS website[9]. Flux measurements were corrected neither for intrinsic extinction/reddening, nor for host contamination. We only report FWHM and velocity shift values for detectable line

---

[8]Note that in Shen et al. (2008b) we only reported high-quality measurements with median S/N> 6 and a reduced $\chi^2 < 5$ for a single-Gaussian fit to the line; here we retain all measurements for completeness.

[9]http://www.sdss.org/dr7/

components (i.e., the fitted line flux is non-zero), except for cases where the line FWHM and velocity offset can be inferred from other lines (such as the narrow Hβ line, whose FWHM and velocity offset are tied to those of the [O III] doublet).

1. SDSS DR7 designation: *hhmmss.ss+ddmmss.s* (J2000.0; truncated coordinates)

2-4. RA and DEC (in decimal degrees, J2000.0), redshift. Here the redshifts are taken from the DR7 quasar catalog (Schneider et al. 2010). Hewett & Wild (2010) provided improved redshifts for SDSS quasars. These improved redshifts are particularly useful for generating coadded spectra, but the cataloged DR7 redshifts are fine for most of the purposes considered here.

5-7. Spectroscopic plate, fiber and Modified Julian date (MJD): the combination of plate-fiber-MJD locates a particular spectroscopic observation in SDSS. The same object can be observed more than once with different plate-fiber-MJD combinations either on a repeated plate (same plate and fiber numbers but different MJD number), or on different plates. The DR7 quasar catalog typically lists the spectroscopic observation with the highest S/N.

8. TARGET_FLAG_TARGET: the target selection flag (TARGET version).

9. $N_{\rm spec}$: number of spectroscopic observations. While we only used the default spectrum in our spectral fitting, this flag indicates if there are multiple spectroscopic observations for each object.

10. Uniform flag. 0=not in the uniform sample[10]; 1=uniformly selected using the target selection algorithm in Richards et al. (2002a), and flux limited to $i = 19.1$ at $z < 2.9$ or $i = 20.2$ at $z > 2.9$; 2=selected by the QSO_HiZ branch only in the uniform target selection (Richards et al. 2002a) and with measured spectroscopic redshift $z < 2.9$ and $i > 19.1$. Objects with uniform flag=2 are selected by the uniform quasar target algorithm, but should not be included in statistical studies; the fraction of such uniform objects is low ($< 1\%$; red dots in Fig. 1).

11. $M_i(z = 2)$: absolute i-band magnitude in the current cosmology, K-corrected to $z = 2$ following[11] Richards et al. (2006b).

---

[10] For more details regarding the uniform sample selection and its sky coverage, see, e.g., Richards et al. (2002a, 2006b); Shen et al. (2007).

[11] The K-corrections here include both continuum K-correction and emission-line K-correction (Richards et al. 2006b); while the cataloged absolute magnitudes in Schneider et al. (2010) were K-corrected for continuum only, assuming a power-law continuum.

12-13. Bolometric luminosity $L_{\rm bol}$ and its error: computed from L_{5100} ($z < 0.7$), L_{3000} ($0.7 \leq z < 1.9$), L_{1350} ($z \geq 1.9$) using the spectral fits and bolometric corrections[12] $BC_{5100} = 9.26$, $BC_{3000} = 5.15$ and $BC_{1350} = 3.81$ from the composite SED in Richards et al. (2006a).

14. BAL flag: 0=nonBALQSO or no wavelength coverage; 1=C IV HiBALQSO; 2=Mg II LoBALQSO; 3=both 1 and 2. The LoBALQSO selection is very incomplete as discussed in §2.

15. FIRST radio flag: -1=not in FIRST footprint; 0=FIRST undetected; 1=core dominant; 2=lobe dominant (for details, see Jiang et al. 2007, and discussion in §2). Note these two classes of radio morphology do not necessarily correspond to the FR I and FR II types (see Lin et al. 2010 for more details).

16-17. *Observed* radio flux density at rest-frame 6 cm $f_{\rm 6cm}$ and optical flux density at rest-frame 2500 Å f_{2500}. Both are in the observed frame.

18. Radio loudness $R \equiv f_{\rm 6cm}/f_{2500}$.

19-24. L_{5100}, L_{3000}, L_{1350} and their errors: continuum luminosity at 5100 Å, 3000 Å and 1350 Å, measured from the spectral fits. No correction for host contamination is made (see discussion in §3.6).

25-30. Line luminosity, FWHM, restframe equivalent width and their errors for the broad Hα component.

31-36. Line luminosity, FWHM, restframe equivalent width and their errors for the narrow Hα component.

37-40. Line luminosity, restframe equivalent width and their errors for narrow [N II] $\lambda 6584$.

41-44. Line luminosity, restframe equivalent width and their errors for narrow [S II] $\lambda 6717$.

45-48. Line luminosity, restframe equivalent width and their errors for narrow [S II] $\lambda 6731$.

---

[12]The SEDs for individual quasars show significant scatter (e.g., Richards et al. 2006a), so the adopted bolometric corrections are only appropriate in the average sense. Some authors suggest to remove the IR bump in the SED in estimating the bolometric corrections (e.g., Marconi et al. 2004), where the IR radiation is assumed to come from the reprocessed UV radiation. This will generally reduce the bolometric corrections by about one third. However, we are not correcting for intrinsic extinction of the flux, and we did not subtract emission line flux in the Richards et al. composite SED when estimating the bolometric corrections, hence using our fiducial bolometric corrections will not overestimate the bolometric luminosity significantly.

49-50. 6000-6500 Å iron restframe equivalent width and its error.

51-52. Power-law slope α_λ and its error for the continuum fit for Hα.

53-54. Number of good pixels and median S/N per pixel for the Hα region (6400-6765 Å).

55. Reduced χ^2 for the Hα line fit; -1 if not fitted.

56-61. Line luminosity, FWHM, restframe equivalent width and their errors for the broad Hβ component.

62-67. Line luminosity, FWHM, restframe equivalent width and their errors for the narrow Hβ component.

68. FWHM of broad Hβ using a single Gaussian fit (Shen et al. 2008b).

69-72. Line luminosity, restframe equivalent width and their errors for [O III] λ4959.

73-76. Line luminosity, restframe equivalent width and their errors for [O III] λ5007.

77-78. 4435-4685 Å iron restframe equivalent width and its error.

79-80. Power-law slope α_λ and its error for the continuum fit for Hβ.

81-82. Number of good pixels and median S/N per pixel for the Hβ region (4750-4950 Å).

83. Reduced χ^2 for the Hβ line fit; -1 if not fitted.

84-89. Line luminosity, FWHM, restframe equivalent width and their errors for the whole Mg II profile.

90-95. Line luminosity, FWHM, restframe equivalent width and their errors for the broad Mg II profile.

96. FWHM of broad Mg II using a single Gaussian fit (Shen et al. 2008b).

97-98. 2200-3090 Å iron restframe equivalent width and its error.

99-100. Power-law slope α_λ and its error for the continuum fit for Mg II.

101-102. Number of good pixels and median S/N per pixel for the Mg II region (2700-2900 Å).

103. Reduced χ^2 for the Mg II line fit; -1 if not fitted.

104-109. Line luminosity, FWHM, restframe equivalent width and their errors for the whole C IV profile.

110-111. Power-law slope α_λ and its error for the continuum fit for C IV.

112-113. Number of good pixels and median S/N per pixel for the C IV region (1500-1600 Å).

114. Reduced χ^2 for the C IV line fit; -1 if not fitted.

115-126. Velocity shifts (and their errors) relative to the systemic redshift (cataloged in Schneider et al. 2010) for broad Hα, narrow Hα, broad Hβ, narrow Hβ, broad Mg II, and C IV. The velocity shifts for the broad lines are measured from the peak of the multiple-Gaussian model fit to the broad component[13]. Recall that the velocity shifts of narrow lines were tied together during spectral fits. These velocity shifts can be used to compute the relative velocity offsets between two lines for the same object, such as the C IV-Mg II blueshift, but should *not* be interpreted as the velocity shifts from the rest-frame of the host galaxy due to uncertainties in the systemic redshift. Positive values indicate blueshift and negative values indicate redshift; value of 3×10^5 indicates an unmeasurable quantity.

127-138. Virial BH masses using calibrations of Hβ (MD04), Hβ (VP06), Mg II (MD04), Mg II (VO09), Mg II (S10) and C IV (VP06). The definitions of the acronym names of each calibration can be found in §3.7. Zero value indicates an unmeasurable quantity. We use FWHMs from a single Gaussian fit to the broad component for Hβ (MD04) and Mg II (MD04); FWHMs from the multiple-Gaussian fit to the broad Hβ for Hβ (VP06); FWHMs from the multiple-Gaussian fit to the entire Mg II and C IV lines for Mg II (VO09) and C IV (VP06) respectively; FWHMs from the multiple-Gaussian fit to the broad Mg II line for Mg II (S10). See §3 for details.

139. The adopted fiducial virial BH mass if more than one estimate is available. See detailed discussion in §3.7.

140. The measurement uncertainty of the adopted fiducial virial BH mass, propagated from the measurement uncertainties of continuum luminosity and FWHM. Note that this uncertainty includes neither the statistical uncertainty ($\gtrsim 0.3 - 0.4$ dex) from virial mass calibrations, nor the systematic uncertainties with these virial BH masses.

141. Eddington ratio computed using the fiducial virial BH mass.

---

[13]The velocity shifts of the broad lines measured from the centroid of a single Gaussian fit to the line on average are consistent with those using the peak of the multiple-Gaussian fit with negligible mean offset, but they can differ (typically by $\lesssim 200$ kms^{-1}) for individual objects.

142. Special interest flag. This is a binary flag: bit#0 set=disk emitters with high confidence (the vast majority are selected based on the Balmer lines); bit#1 set=disk emitter candidates; bit#2 set=double-peaked [O III] $\lambda\lambda$4959,5007 lines. These flags were set upon visual inspection of all $z < 0.89$ quasars in the catalog. In particular, disk emitter candidates (bit#1=1) are those with asymmetric broad Balmer line profile or systematic velocity shifts from the narrow lines; while those with high confidence (bit#0=1) show unambiguous double-peaked (or highly asymmetric) broad line profile or large velocity offsets between the broad and narrow lines. Fig. 11 shows two examples of disk emitters with high confidence. We call these objects "disk emitters" even though some of them may be explained by alternative scenarios, such as a close SMBH binary (e.g., see discussion in Shen & Loeb 2010).

4. Applications

The spectral measurements described above can be used to study the statistical properties of broad line quasars. Here we briefly discuss some applications of this spectral catalog.

4.1. Correlations between emission line properties

One great virtue of the SDSS DR7 quasar survey is that it provides unprecedented statistics for broad-line quasar properties. To demonstrate this, Figs. 12-14 show some statistical properties of quasars using our spectral measurements for Hβ, Mg II, and C IV, respectively. These figures show the typical values of these properties for SDSS quasars as a quick reference.

There are correlations among the properties shown in Figs. 12-14. Some of these correlations are not due to selection effects. For instance, the well-known Baldwin effect (Baldwin 1977), i.e., the anti-correlation between line EW and continuum luminosity, is clearly seen for C IV and Mg II. There are also strong correlations between EW and FWHM for Mg II (e.g., Dong et al. 2009b) and C IV, which are not due to any apparent selection effects. The statistics of our catalog now allows in-depth investigations of these correlations when binning in different quantities such as redshift or luminosity, and to probe the origins of these correlations. However, there are some apparent correlations which are likely due to selection effects inherent in a flux-limited sample, or host contamination. For instance, the apparent anti-correlation between α_λ and $\log L_{5100}$, and the mild negative Baldwin effect below $\log L_{5100} \lesssim 45$ for Hβ seen in Fig. 12, are most likely caused by increasing host contamination towards fainter
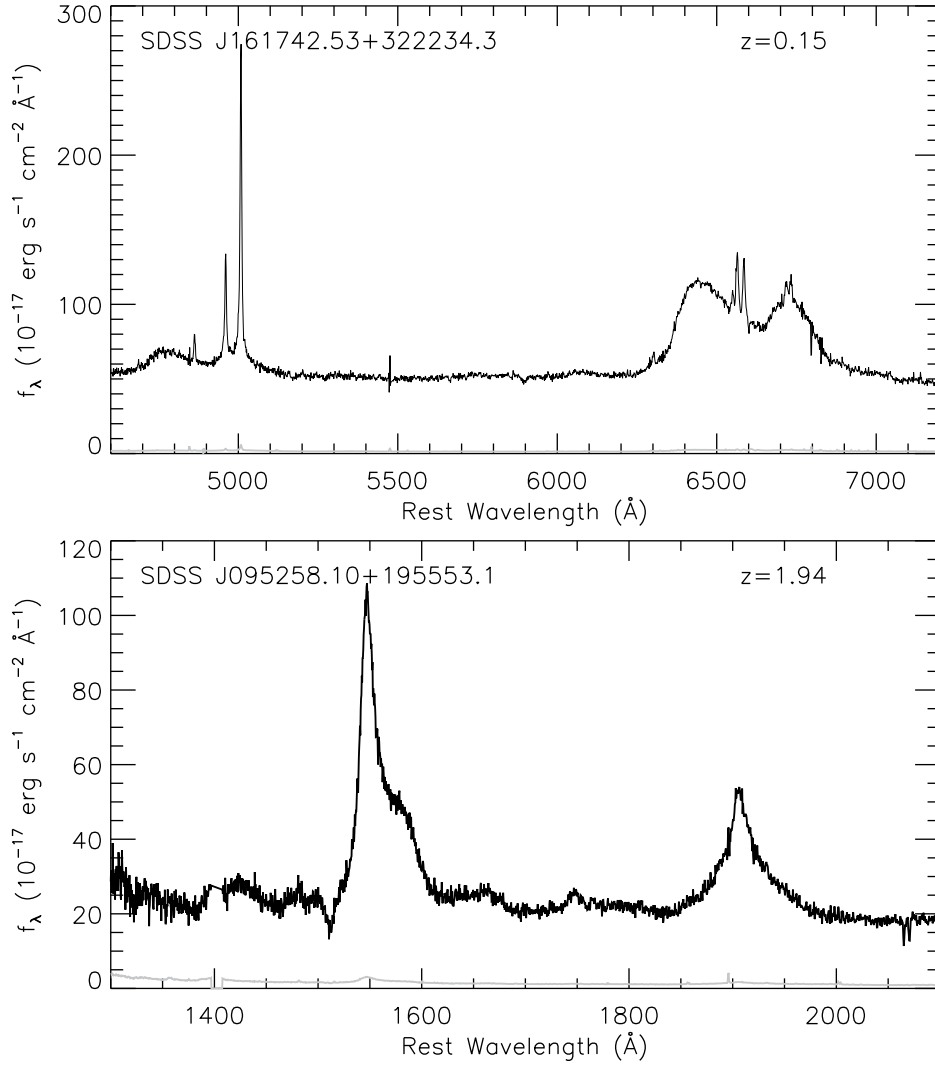
Fig. 11.— Two examples of disk emitters with high confidence (bit#0=1). *Upper:* a Balmer disk emitter at $z = 0.15$. *Bottom:* a possible CIV disk emitter at $z = 1.94$.
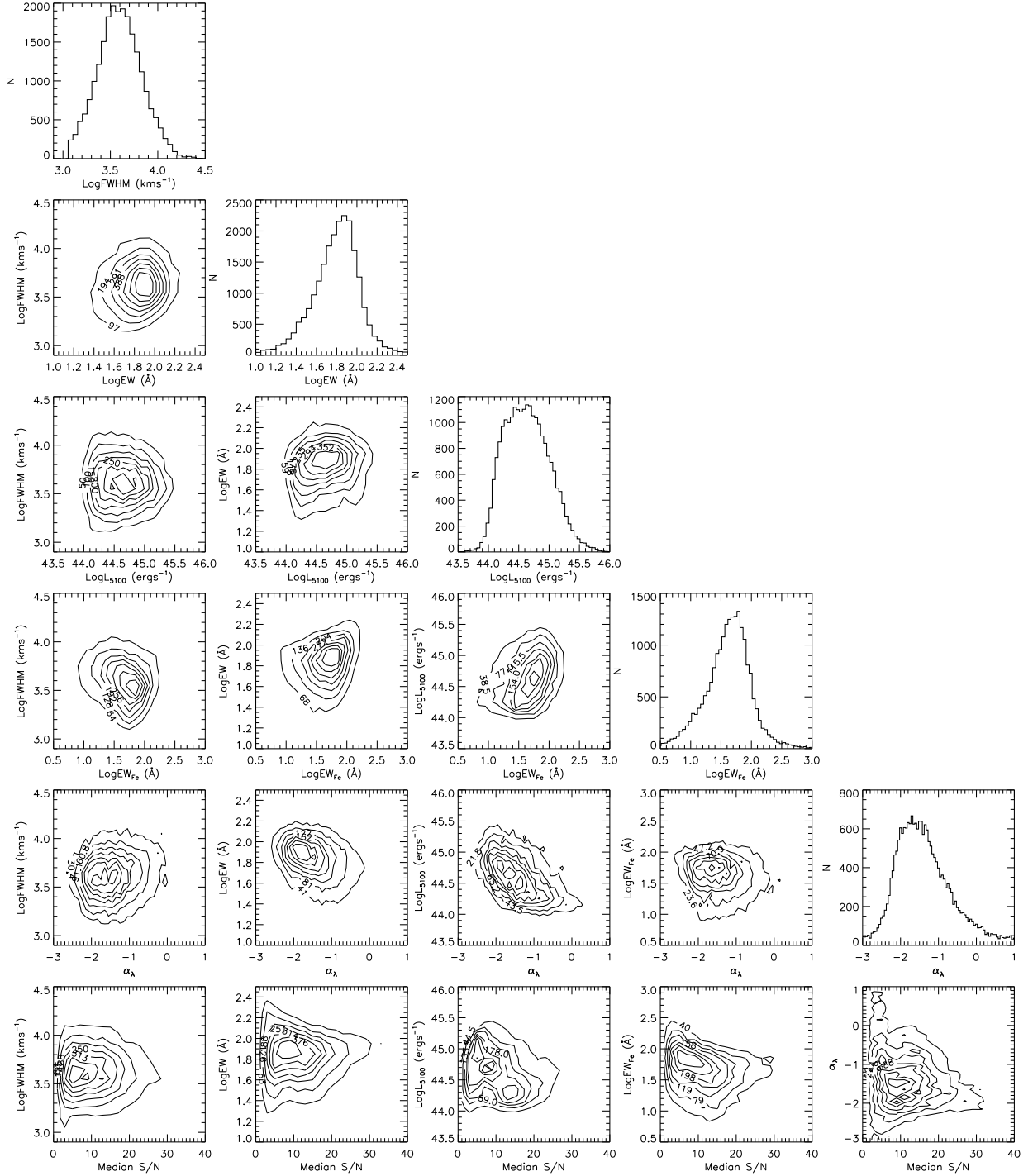
Fig. 12.— Statistical properties for Hβ based on our spectral measurements (for all quasars). Contours are local point density contours estimated with a grid size of Δ = 0.1 on both axes (Δ = 2 on the median S/N axis). Contour levels are equally spaced linearly with their values marked for the outermost several contours. The strong anti-correlation between the power-law continuum slope and luminosity reflects the increasing host galaxy contamination towards fainter quasar luminosites (see §3.6 and Fig. 9).
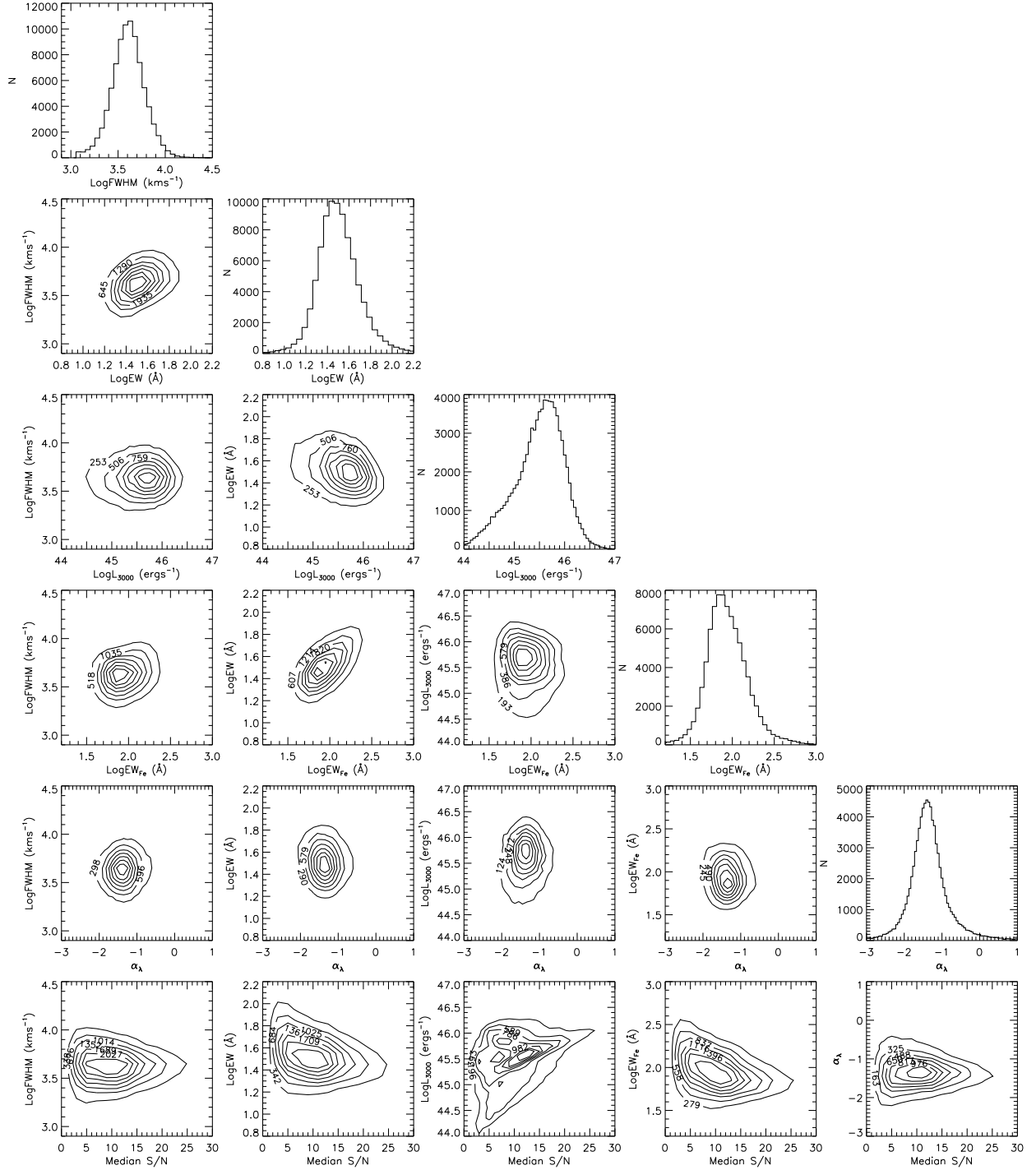
Fig. 13.— Statistical properties for Mg_II based on our spectral measurements (for all quasars). Contours are local point density contours estimated with a grid size of $\Delta = 0.1$ on both axes ($\Delta = 2$ on the median S/N axis). Contour levels are equally spaced linearly with their values marked for the outermost several contours. There are several known correlations, such as the Mg_II Baldwin effect (e.g., Baldwin 1977; Croom et al. 2002), and the correlation between FWHM and EW (e.g., Dong et al. 2009a).
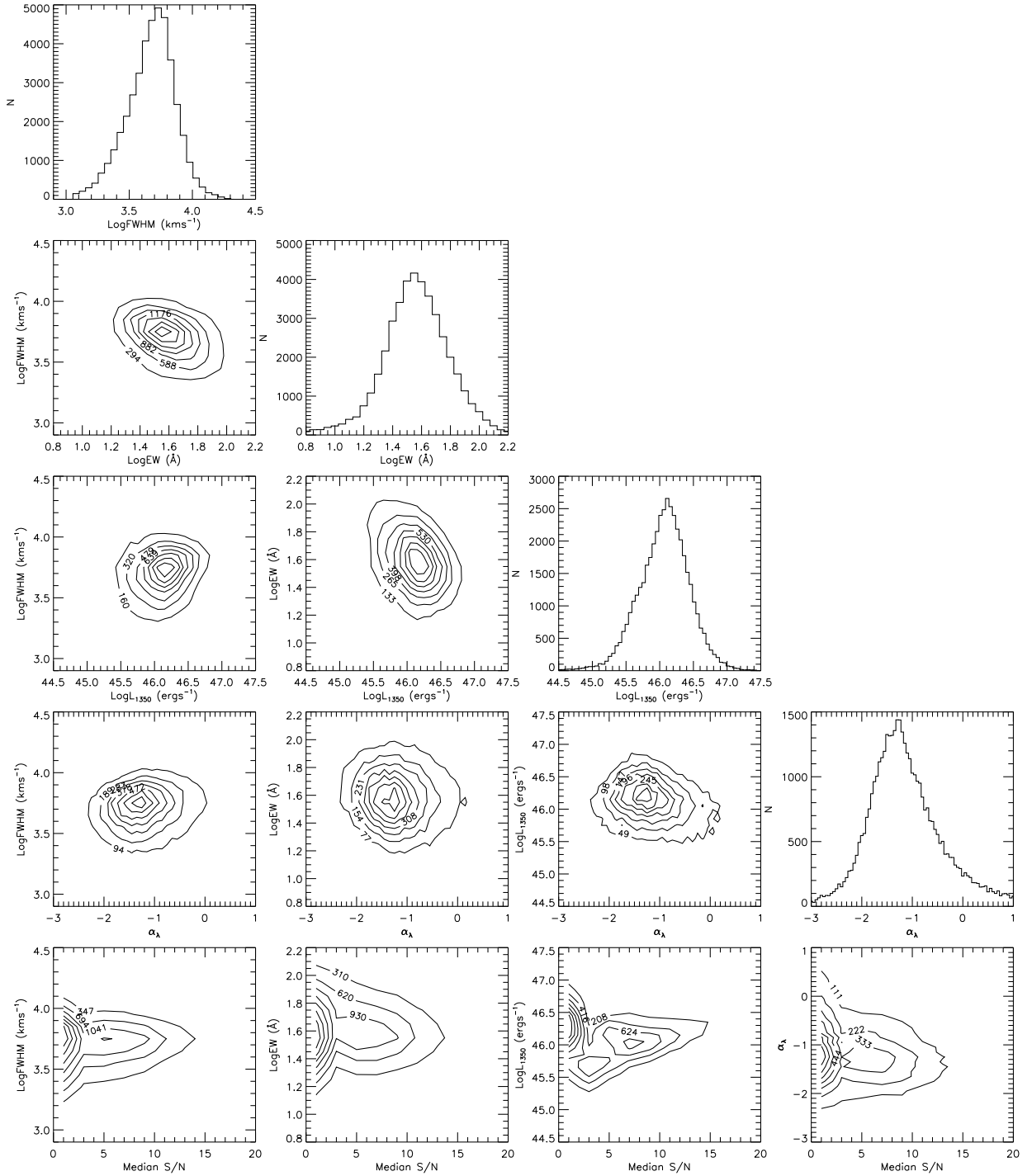
Fig. 14.— Statistical properties for C IV based on our spectral measurements (for all quasars). Contours are local point density contours estimated with a grid size of $\Delta = 0.1$ on both axes ($\Delta = 2$ on the median S/N axis). Contour levels are equally spaced linearly with their values marked for the outermost several contours. There are several correlations involving EW, FWHM and luminosity that may be different manifestations of the same phenomenon (e.g., Baldwin 1977; Richards et al. 2002b). The clustering of a population of low S/N objects is caused by the quasar target selection, i.e., quasars are targeted to a fainter limiting magnitude at $z \gtrsim 2.9$ (see Fig. 1).

luminosities (see §3.6). Moreover, the spectral quality (mainly S/N) has important effects on the measured quantities and may bias the measurements at the low S/N end. Thus one must take these issues into account when using the catalog to study correlations among various properties. The detailed investigations of various correlations will be presented elsewhere.

Fig. 15 shows the so-called 4DE1 projection in the Hβ FWHM versus $R_{\mathrm{FeII}} = \mathrm{EW}_{\mathrm{FeII}4434-4684}/\mathrm{EW}_{\mathrm{H}\beta}$ space (e.g., Sulentic et al. 2000, 2002; Zamfir et al. 2010), which is an extension of the eigenvector space for quasar properties suggested by Boroson & Green (1992). Objects with Hβ FWHM > 4000 km s^{-1} (i.e., population "B" in the terminology of the 4DE1 parameter space of Sulentic and collaborators) have a tendency to have weaker relative iron emission strength for larger FWHMs. The black contours show the distribution of all quasars while the red contours show the distribution of radio-loud ($R > 10$) quasars. It appears that the radio-loud contours are more vertically elongated, broadly consistent with the phenomenological classification scheme based on the 4DE1 parameter space (e.g., Sulentic et al. 2000, 2002; Zamfir et al. 2010). The physics driving these characteristics in the parameter space is currently not clear, and deserves further study.

Fig. 16 shows the correlation between the [O III] λ5007 luminosity and the continuum luminosity at 5100 Å. This correlation is usually used to estimate the bolometric luminosity using the [O III] λ5007 luminosity as a surrogate for type 2 quasars (e.g, Kauffmann et al. 2003; Zakamska et al. 2003; Heckman et al. 2004; Reyes et al. 2008). While the correlation is apparent, it has a large scatter, as noted in earlier studies (e.g., Heckman et al. 2004; Reyes et al. 2008). The mean linear relation is:

$$\log L_{\mathrm{[OIII]}\lambda5007} \approx \log L_{5100} - 2.5 \; , \tag{15}$$

with a scatter ~ 0.35 dex. Using the bolometric correction from Richards et al. (2006a), a crude conversion between $L_{\mathrm{[OIII]}\lambda5007}$ and the quasar bolometric luminosity is: $L_{\mathrm{bol}} \approx 3200 L_{\mathrm{[OIII]}\lambda5007}$.

4.2. Emission line shifts

Fig. 17 shows the distributions of velocity shifts between various emission lines. Recall that the velocity of the broad lines is measured from the peak of the multiple-Gaussian fit. The left panel of Fig. 17 shows the distributions of velocity shifts between the broad Balmer lines and the narrow lines. The means of these distributions are consistent with zero, hence there is no offset in the mean between the broad and narrow Balmer lines (cf., Bonning et al. 2007). We note that if we did not account for the blue wings of the narrow [O III] $\lambda\lambda$4959,5007 lines during spectral fitting, there would be a net redshift of the order of
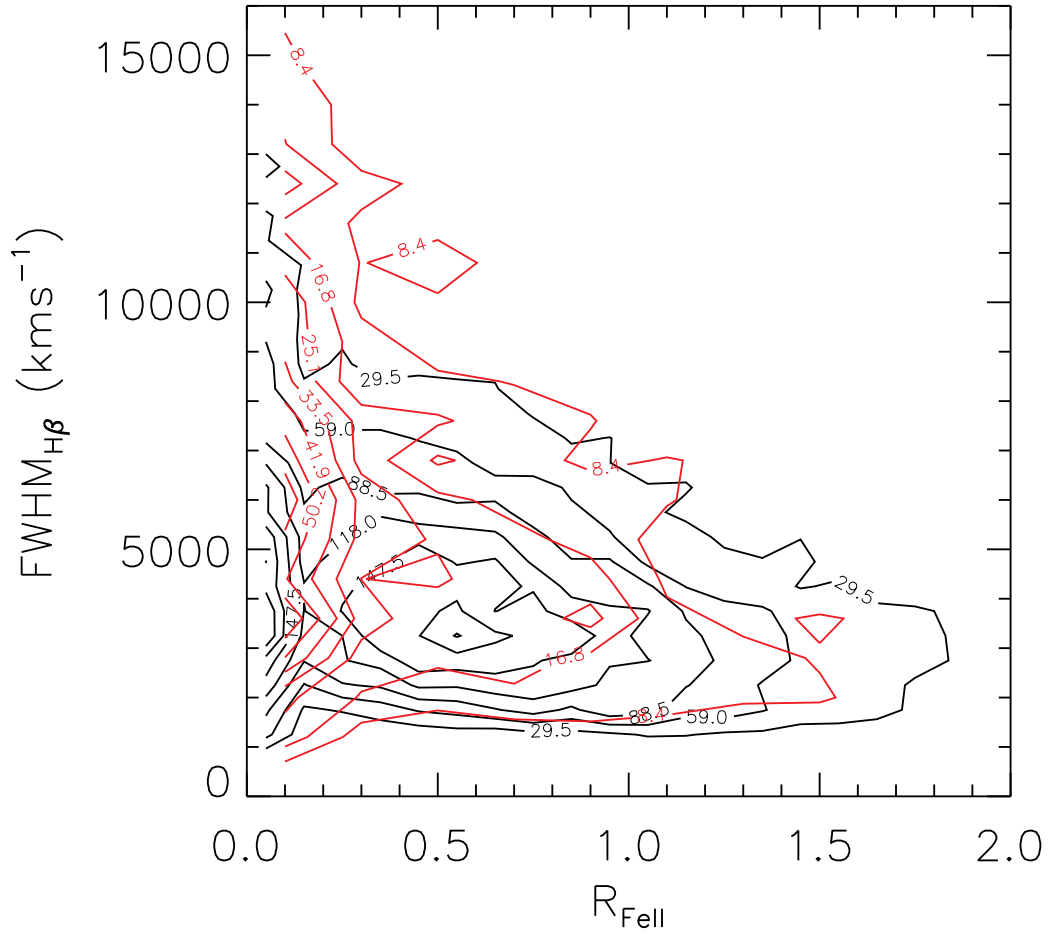
Fig. 15.— Distribution of quasars in the projected 4DE1 parameter space (e.g., Sulentic et al. 2000). Contours are local point density contours estimated with a grid size of $\Delta_x/\Delta_y = 0.1/500$ (black) and $\Delta_x/\Delta_y = 0.2/800$ (red), where the black contours are for all quasars and the red contours are for radio-loud $(R > 10)$ quasars only.
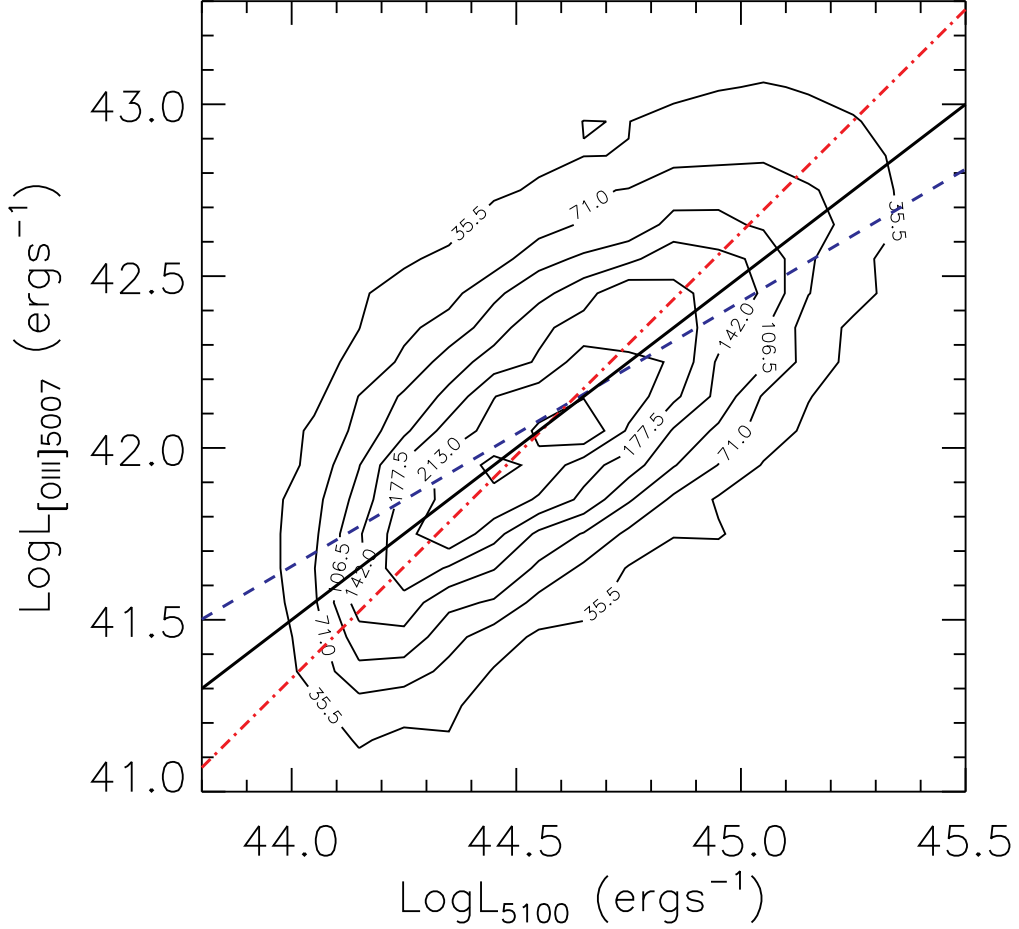
Fig. 16.— Correlation between $L_{[OIII]5007}$ and L_{5100}. Contours are local point density contours estimated with a grid size of $\Delta = 0.1$ on both axes. The dashed line is the linear regression fit treating $\log L_{5100}$ as the independent variable; the best-fit relation is $\log(L_{[OIII]5007}/\mathrm{erg\,s}^{-1}) = 7.76 + 0.77 \log(L_{5100}/\mathrm{erg\,s}^{-1})$ and the scatter around this relation is ~ 0.38 dex. The dash-dotted line is the bisector linear regression fit; the best-fit relation is $\log(L_{[OIII]5007}/\mathrm{erg\,s}^{-1}) = -17.54 + 1.34 \log(L_{5100}/\mathrm{erg\,s}^{-1})$ and the scatter around this relation is ~ 0.4 dex. The solid line is the mean linear relation described in Eqn. (15).

~ 100 km s^{-1} between the broad Hβ line and [O III], which is inconsistent with the results for Hα versus [S II]. The right panel of Fig. 17 shows the velocity offsets between Mg II and [O III] and between C IV and Mg II. The Mg II line shows no mean offset from [O III], while the C IV line shows a systematic blueshift of ~ 600 km s^{-1} with respect to Mg II (e.g., Gaskell 1982; Tytler & Fan 1992; Richards et al. 2002b); see Richards et al. (2011) for further discussion.

It is interesting to note that many of the objects in the wings of the velocity offset distributions of the broad Balmer lines vs the narrow lines are either strong disk-emitters (e.g., Chen et al. 1989; Eracleous & Halpern 1994; Strateva et al. 2003), or have the broad component systematically offset from the narrow line center; in other cases the apparent large shifts were caused by poor fits to noisy spectra.

5. Summary

We have constructed an SDSS DR7 quasar catalog in which we tabulate various properties. In this catalog we compiled continuum and emission line properties for Hα, Hβ, Mg II, and C IV based on our spectral fits. We also included radio properties, and flagged quasars of special interest, such as broad absorption line quasars and disk emitters. We also compiled virial BH mass estimates using these spectral measurements. This catalog can be used to study correlations among properties of optically selected quasars, and the active black hole mass function in quasars (Shen et al., in preparation). We performed various tests and found that our automatic fitting procedure to emission lines performed reasonably well. However, one must take into account the possible effects of selection and S/N, as well as the systematics involved in converting the measured quantities to derived quantities, when using these measurements to study quasar properties. In particular, we *do not* encourage direct interpretations based on derived quantities (such as virial BH masses and bolometric luminosity) without accounting for the difference between the estimated value and the true value for these quantities. Such direct interpretations will usually lead to biased or even spurious results.

We make this catalog publicly available online[14], where we also provide supplemental materials (such as dereddened spectra, quality assessment fitting plots, etc) and important future updates of this compilation.

We thank the anonymous referee for constructive comments that improved the manuscript.

---

[14]http://www.cfa.harvard.edu/~yshen/BH_mass/dr7.htm

Facilities: Sloan

REFERENCES

Abazajian, K. N., et al. 2009, ApJS, 182, 543

Adelman-McCarthy, J. K., et al. 2008, ApJS, 175, 297

Akritas, M. G., & Bershady, M. A. 1996, ApJ, 470, 706

Bachev, R., Marziani, P., Sulentic, J. W., Zamanov, R., Calvani, M., & Dultzin-Hacyan, D. 2004, ApJ, 617, 171

Baldwin, J. A. 1977, ApJ, 214, 679

Baskin, A., & Laor, A. 2005, MNRAS, 356, 1029

Blanton, M. R., Lin, H., Lupton, R. H., Maley, F. M., Young, N., Zehavi, I., & Loveday, J. 2003, AJ, 125, 2276

Bonning, E. W., Shields, G. A., & Salviander, S. 2007, ApJ, 666, L13

Boroson, T. A., & Green, R. F. 1992, ApJS, 80, 109

Cardelli, J. A., Clayton, G. C., & Mathis, J. S. 1989, ApJ, 345, 245

Chen, K., Halpern, J. P., & Filippenko, A. V. 1989, ApJ, 339, 742

Collin, S., Kawaguchi, T., Peterson, B. M., & Vestergaard, M. 2006, A&A, 456, 75

Croom, S. M., et al. 2002, MNRAS, 337, 275

Croom, S. M., Smith, R. J., Boyle, B. J., Shanks, T., Miller, L., Outram, P. J., & Loaring, N. S. 2004, MNRAS, 349, 1397

Denney, K. D., et al. 2009, ApJ, 704, L80

Dietrich, M., & Hamann, F. 2004, ApJ, 611, 761

Dong, X., Wang, J., Wang, T., Wang, H., Fan, X., Zhou, H., & Yuan, W. 2009a, ArXiv e-prints

Dong, X., Wang, T., Wang, J., Fan, X., Wang, H., Zhou, H., & Yuan, W. 2009b, ApJ, 703, L1

Eracleous, M., & Halpern, J. P. 1994, ApJS, 90, 1

Fine, S., et al. 2008, MNRAS, 390, 1413

—. 2006, MNRAS, 373, 613

Fukugita, M., Ichikawa, T., Gunn, J. E., Doi, M., Shimasaku, K., & Schneider, D. P. 1996, AJ, 111, 1748

Gaskell, C. M. 1982, ApJ, 263, 79

Gaskell, C. M. 2010, Nature, 463, 1

Gibson, R. R., et al. 2009, ApJ, 692, 758

Graham, A. W., Onken, C. A., Athanassoula, E., & Combes, F. 2011, MNRAS, in press, arXiv:1007.3834

Greene, J. E., & Ho, L. C. 2005a, ApJ, 627, 721

—. 2005b, ApJ, 630, 122

Gunn, J. E., et al. 1998, AJ, 116, 3040

—. 2006, AJ, 131, 2332

Hao, L., et al. 2005, AJ, 129, 1783

Heckman, T. M., Miley, G. K., van Breugel, W. J. M., & Butcher, H. R. 1981, ApJ, 247, 403

Heckman, T. M., Kauffmann, G., Brinchmann, J., Charlot, S., Tremonti, C., & White, S. D. M. 2004, ApJ, 613, 109

Hewett, P. C. & Wild, V. 2010, MNRAS, 405, 2302

Hogg, D. W., Finkbeiner, D. P., Schlegel, D. J., & Gunn, J. E. 2001, AJ, 122, 2129

Hopkins, P. F., Hernquist, L., Cox, T. J., Di Matteo, T., Robertson, B., & Springel, V. 2006, ApJS, 163, 1

Hopkins, P. F., Hernquist, L., Cox, T. J., & Kereš, D. 2008, ApJS, 175, 356

Hu, C., Wang, J., Ho, L. C., Chen, Y., Bian, W., & Xue, S. 2008a, ApJ, 683, L115

Hu, C., Wang, J., Ho, L. C., Chen, Y., Zhang, H., Bian, W., & Xue, S. 2008b, ApJ, 687, 78

Ivezić, Ž., et al. 2004, Astronomische Nachrichten, 325, 583

Jiang, L., Fan, X., Ivezić, Ž., Richards, G. T., Schneider, D. P., Strauss, M. A., & Kelly, B. C. 2007, ApJ, 656, 680

Kauffmann, G., & Haehnelt, M. 2000, MNRAS, 311, 576

Kauffmann, G., et al. 2003, MNRAS, 341, 33

Kelly, B. C., Vestergaard, M., & Fan, X. 2009, ApJ, 692, 1388

Kollmeier, J. A., et al. 2006, ApJ, 648, 128

Komossa, S., Xu, D., Zhou, H., Storchi-Bergmann, T., & Binette, L. 2008, ApJ, 680, 926

Lin, Y.-T., Shen, Y., Strauss, M. A., Richards, G. T., & Lunnan, R. 2010, ApJ, 723, 1119

Liu, X., Shen, Y., Strauss, M. A., & Greene, J. E. 2010a, ApJ, 708, 427

Liu, X., Greene, J. E., Shen, Y., & Strauss, M. A. 2010b, ApJ, 715, L30

Lupton, R., Gunn, J. E., Ivezić, Z., Knapp, G. R., & Kent, S. 2001, in Astronomical Society of the Pacific Conference Series, Vol. 238, Astronomical Data Analysis Software and Systems X, ed. F. R. Harnden, Jr., F. A. Primini, & H. E. Payne, 269

Marconi, A., Axon, D. J., Maiolino, R., Nagao, T., Pastorini, G., Pietrini, P., Robinson, A., & Torricelli, G. 2008, ApJ, 678, 693

Marconi, A., Risaliti, G., Gilli, R., Hunt, L. K., Maiolino, R., & Salvati, M. 2004, MNRAS, 351, 169

Marziani, P., Sulentic, J. W., Dultzin-Hacyan, D., Calvani, M., & Moles, M. 1996, ApJS, 104, 37

McGill, K. L., Woo, J., Treu, T., & Malkan, M. A. 2008, ApJ, 673, 703

McLure, R. J., & Dunlop, J. S. 2004, MNRAS, 352, 1390 (MD04)

McLure, R. J., & Jarvis, M. J. 2002, MNRAS, 337, 109

Onken, C. A., Ferrarese, L., Merritt, D., Peterson, B. M., Pogge, R. W., Vestergaard, M., & Wandel, A. 2004, ApJ, 615, 645

Onken, C. A., & Kollmeier, J. A. 2008, ApJ, 689, L13

Pier, J. R., Munn, J. A., Hindsley, R. B., Hennessy, G. S., Kent, S. M., Lupton, R. H., & Ivezić, Ž. 2003, AJ, 125, 1559

Rafiee, A., & Hall, P. B. 2010, ApJS, submitted

Reyes, R., et al. 2008, AJ, 136, 2373

Richards, G. T., et al. 2002a, AJ, 123, 2945

—. 2006a, ApJS, 166, 470

—. 2006b, AJ, 131, 2766

Richards, G. T., Vanden Berk, D. E., Reichard, T. A., Hall, P. B., Schneider, D. P., SubbaRao, M., Thakar, A. R., & York, D. G. 2002b, AJ, 124, 1

Richards, G. T., et al. 2011, AJ, submitted, arXiv:1011.2282

Salviander, S., Shields, G. A., Gebhardt, K., & Bonning, E. W. 2007, ApJ, 662, 131

Schlegel, D. J., Finkbeiner, D. P., & Davis, M. 1998, ApJ, 500, 525

Schneider, D. P., et al. 2007, AJ, 134, 102

—. 2010, AJ, 139, 2360

Shankar, F., Weinberg, D. H., & Miralda-Escudé, J. 2009, ApJ, 690, 20

Shen, J., Vanden Berk, D. E., Schneider, D. P., & Hall, P. B. 2008a, AJ, 135, 928

Shen, Y. 2009, ApJ, 704, 89

Shen, Y., Greene, J. E., Strauss, M. A., Richards, G. T., & Schneider, D. P. 2008b, ApJ, 680, 169

Shen, Y., Liu, X., Greene, J. E., & Strauss, M. A. 2011, ApJ, submitted, arXiv:1011.5246

Shen, Y., & Kelly, B. C. 2010, ApJ, 713, 41

Shen, Y., & Loeb, A. 2010, ApJ, 725, 249

Shen, Y., et al. 2007, AJ, 133, 2222

Smith, J. A., et al. 2002, AJ, 123, 2121

Smith, K. L., Shields, G. A., Bonning, E. W., McMullen, C. C., & Salviander, S. 2010, 716, 866

Stoughton, C., et al. 2002, AJ, 123, 485

Strateva, I. V., et al. 2003, AJ, 126, 1720

Sulentic, J. W., Bachev, R., Marziani, P., Negrete, C. A., & Dultzin, D. 2007, ApJ, 666, 757

Sulentic, J. W., Marziani, P., Zamanov, R., Bachev, R., Calvani, M., & Dultzin-Hacyan, D. 2002, ApJ, 566, L71

Sulentic, J. W., Zwitter, T., Marziani, P., & Dultzin-Hacyan, D. 2000, ApJ, 536, L5

Tucker, D. L., et al. 2006, Astronomische Nachrichten, 327, 821

Tytler, D., & Fan, X. 1992, ApJS, 79, 1

van der Marel, R. P., & Franx, M. 1993, ApJ, 407, 525

Vanden Berk, D. E., et al. 2001, AJ, 122, 549

Vestergaard, M. 2002, ApJ, 571, 733

Vestergaard, M., & Osmer, P. S. 2009, ApJ, 699, 800 (VO09)

Vestergaard, M., & Peterson, B. M. 2006, ApJ, 641, 689 (VP06)

Vestergaard, M., & Wilkes, B. J. 2001, ApJS, 134, 1

Wang, J., Chen, Y., Hu, C., Mao, W., Zhang, S., & Bian, W. 2009a, ApJ, 705, L76

Wang, J., et al. 2009b, ApJ, 707, 1334

White, R. L., Becker, R. H., Helfand, D. J., & Gregg, M. D. 1997, ApJ, 475, 479

Woo, J.-H., et al. 2010, ApJ, 716, 269

Wu, X.-B., Wang, R., Kong, M. Z., Liu, F. K, & Han, J. L. 2004, A&A, 424, 793

Wu, J., Vanden Berk, D. E., Brandt, W. N., Schneider, D. P., Gibson, R. R., & Wu, J. 2009, ApJ, 702, 767

Wyithe, J. S. B., & Loeb, A. 2003, ApJ, 595, 614

York, D. G., et al. 2000, AJ, 120, 1579

Zakamska, N. L., et al. 2003, AJ, 126, 2125

Zamfir, S., Sulentic, J. W., Marziani, P., & Dultzin, D. 2010, MNRAS, 403, 1759

Table 1:: FITS Catalog Format

Column	Format	Description
1	STRING	SDSS DR7 designation hhmmss.ss+ddmmss.s (J2000.0)
2	DOUBLE	Right ascension in decimal degrees (J2000.0)
3	DOUBLE	Declination in decimal degrees (J2000.0)
4	DOUBLE	Redshift
5	LONG	Spectroscopic plate number
6	LONG	Spectroscopic fiber number
7	LONG	MJD of spectroscopic observation
8	LONG	Target selection flag (TARGET version)
9	LONG	Number of spectroscopic observations
10	LONG	Uniform selection flag
11	DOUBLE	$M_i(z = 2)$ [$h = 0.7$, $\Omega_0 = 0.3$, $\Omega_\Lambda = 0.7$, K-corrected to $z = 2$, following Richards et al. (2006b)]
12	DOUBLE	Bolometric luminosity [$\log(L_{\rm bol}/{\rm ergs}^{-1})$]
13	DOUBLE	Uncertainty in $\log L_{\rm bol}$
14	LONG	BAL flag (0=nonBALQSO or no wavelength coverage; 1=CIV BALQSO; 2=MgII BALQSO; 3=both 1 and 2)
15	LONG	FIRST radio flag (-1=not in FIRST footprint; 0=FIRST undetected; 1=core-dominant; 2=lobe-dominant)

This preprint was prepared with the AAS LaTeX macros v5.2.

Table 1 – Continued

Column	Format	Description
16	DOUBLE	Observed radio flux density at rest-frame 6 cm $f_{\nu,6cm}$ [mJy]
17	DOUBLE	Observed optical flux density at rest-frame 2500Å [$\log(f_{\nu,2500}/\mathrm{ergs}^{-1}\mathrm{cm}^{-2}\mathrm{Hz}^{-1})$]
18	DOUBLE	Radio loudness $R \equiv f_{\nu,6cm}/f_{\nu,2500}$
19	DOUBLE	Monochromatic luminosity at 5100Å [$\log(L_{5100}/\mathrm{ergs}^{-1})$]
20	DOUBLE	Uncertainty in $\log L_{5100}$
21	DOUBLE	Monochromatic luminosity at 3000Å [$\log(L_{3000}/\mathrm{ergs}^{-1})$]
22	DOUBLE	Uncertainty in $\log L_{3000}$
23	DOUBLE	Monochromatic luminosity at 1350Å [$\log(L_{1350}/\mathrm{ergs}^{-1})$]
24	DOUBLE	Uncertainty in $\log L_{1350}$
25	DOUBLE	Line luminosity of broad Hα [$\log(L/\mathrm{ergs}^{-1})$]
26	DOUBLE	Uncertainty in $\log L_{\mathrm{H}\alpha,\mathrm{broad}}$
27	DOUBLE	FWHM of broad Hα (kms^{-1})
28	DOUBLE	Uncertainty in the broad Hα FWHM
29	DOUBLE	Restframe equivalent width of broad Hα (Å)
30	DOUBLE	Uncertainty in EW$_{\mathrm{H}\alpha,\mathrm{broad}}$
31	DOUBLE	Line luminosity of narrow Hα [$\log(L/\mathrm{ergs}^{-1})$]
32	DOUBLE	Uncertainty in $\log L_{\mathrm{H}\alpha,\mathrm{narrow}}$
33	DOUBLE	FWHM of narrow Hα (kms^{-1})
34	DOUBLE	Uncertainty in the narrow Hα FWHM
35	DOUBLE	Restframe equivalent width of narrow Hα (Å)
36	DOUBLE	Uncertainty in EW$_{\mathrm{H}\alpha,\mathrm{narrow}}$
37	DOUBLE	Line luminosity of [N II] $\lambda6584$ [$\log(L/\mathrm{ergs}^{-1})$]
38	DOUBLE	Uncertainty in $\log L_{\mathrm{[NII]}6584}$
39	DOUBLE	Restframe equivalent width of [N II] $\lambda6584$ (Å)
40	DOUBLE	Uncertainty in EW$_{\mathrm{[NII]}6584}$
41	DOUBLE	Line luminosity of [S II] $\lambda6717$ [$\log(L/\mathrm{ergs}^{-1})$]
42	DOUBLE	Uncertainty in $\log L_{\mathrm{[SII]}6717}$
43	DOUBLE	Restframe equivalent width of [S II] $\lambda6717$ (Å)
44	DOUBLE	Uncertainty in EW$_{\mathrm{[SII]}6717}$
45	DOUBLE	Line luminosity of [S II] $\lambda6731$ [$\log(L/\mathrm{ergs}^{-1})$]
46	DOUBLE	Uncertainty in $\log L_{\mathrm{[SII]}6731}$
47	DOUBLE	Restframe equivalent width of [S II] $\lambda6731$ (Å)
48	DOUBLE	Uncertainty in EW$_{\mathrm{[SII]}6731}$
49	DOUBLE	Restframe equivalent width of Fe within 6000-6500Å (Å)
50	DOUBLE	Uncertainty in EW$_{\mathrm{Fe},\mathrm{H}\alpha}$
51	DOUBLE	Power-law slope for the continuum fit for Hα
52	DOUBLE	Uncertainty in $\alpha_{\mathrm{H}\alpha}$
53	LONG	Number of good pixels for the restframe 6400-6765Å region
54	DOUBLE	Median S/N per pixel for the restframe 6400-6765Å region
55	DOUBLE	Reduced χ^2 for the Hα line fit; -1 if not fitted
56	DOUBLE	Line luminosity of broad Hβ [$\log(L/\mathrm{ergs}^{-1})$]
57	DOUBLE	Uncertainty in $\log L_{\mathrm{H}\beta,\mathrm{broad}}$
58	DOUBLE	FWHM of broad Hβ (kms^{-1})
59	DOUBLE	Uncertainty in the broad Hβ FWHM
60	DOUBLE	Restframe equivalent width of broad Hβ (Å)
61	DOUBLE	Uncertainty in EW$_{\mathrm{H}\beta,\mathrm{broad}}$
62	DOUBLE	Line luminosity of narrow Hβ [$\log(L/\mathrm{ergs}^{-1})$]
63	DOUBLE	Uncertainty in $\log L_{\mathrm{H}\beta,\mathrm{narrow}}$
64	DOUBLE	FWHM of narrow Hβ (kms^{-1})
65	DOUBLE	Uncertainty in the narrow Hβ FWHM
66	DOUBLE	Restframe equivalent width of narrow Hβ (Å)
67	DOUBLE	Uncertainty in EW$_{\mathrm{H}\beta,\mathrm{narrow}}$
68	DOUBLE	FWHM of broad Hβ using a single Gaussian fit (kms^{-1})
69	DOUBLE	Line luminosity of [O III] $\lambda4959$ [$\log(L/\mathrm{ergs}^{-1})$]
70	DOUBLE	Uncertainty in $\log L_{\mathrm{[OIII]}4959}$
71	DOUBLE	Restframe equivalent width of [O III] $\lambda4959$ (Å)
72	DOUBLE	Uncertainty in EW$_{\mathrm{[OIII]}4959}$
73	DOUBLE	Line luminosity of [O III] $\lambda5007$ [$\log(L/\mathrm{ergs}^{-1})$]
74	DOUBLE	Uncertainty in $\log L_{\mathrm{[OIII]}5007}$
75	DOUBLE	Restframe equivalent width of [O III] $\lambda5007$ (Å)
76	DOUBLE	Uncertainty in EW$_{\mathrm{[OIII]}5007}$
77	DOUBLE	Restframe equivalent width of Fe within 4435-4685Å (Å)
78	DOUBLE	Uncertainty in EW$_{\mathrm{Fe},\mathrm{H}\beta}$
79	DOUBLE	Power-law slope for the continuum fit for Hβ
80	DOUBLE	Uncertainty in $\alpha_{\mathrm{H}\beta}$
81	LONG	Number of good pixels for the restframe 4750-4950Å region
82	DOUBLE	Median S/N per pixel for the restframe 4750-4950Å region
83	DOUBLE	Reduced χ^2 for the Hβ line fit; -1 if not fitted
84	DOUBLE	Line luminosity of the whole MgII [$\log(L/\mathrm{ergs}^{-1})$]
85	DOUBLE	Uncertainty in $\log L_{\mathrm{MgII},\mathrm{whole}}$
86	DOUBLE	FWHM of the whole MgII (kms^{-1})
87	DOUBLE	Uncertainty in the whole MgII FWHM

Table 1 – Continued

| Column	Format	Description
88	DOUBLE	Restframe equivalent width of the whole MgII (Å)
89	DOUBLE	Uncertainty in $EW_{MgII,whole}$
90	DOUBLE	Line luminosity of broad MgII [$\log(L/ergs^{-1})$]
91	DOUBLE	Uncertainty in $\log L_{MgII,broad}$
92	DOUBLE	FWHM of broad MgII (kms^{-1})
93	DOUBLE	Uncertainty in the broad MgII FWHM
94	DOUBLE	Restframe equivalent width of broad MgII (Å)
95	DOUBLE	Uncertainty in $EW_{MgII,broad}$
96	DOUBLE	FWHM of broad MgII using a single Gaussian fit (kms^{-1})
97	DOUBLE	Restframe equivalent width of Fe within 2200-3090Å (Å)
98	DOUBLE	Uncertainty in $EW_{Fe,MgII}$
99	DOUBLE	Power-law slope for the continuum fit for MgII
100	DOUBLE	Uncertainty in α_{MgII}
101	LONG	Number of good pixels for the restframe 2700-2900Å region
102	DOUBLE	Median S/N per pixel for the restframe 2700-2900Å region
103	DOUBLE	Reduced χ^2 for the MgII line fit; -1 if not fitted
104	DOUBLE	Line luminosity of the whole CIV [$\log(L/ergs^{-1})$]
105	DOUBLE	Uncertainty in $\log L_{CIV}$
106	DOUBLE	FWHM of the whole CIV (kms^{-1})
107	DOUBLE	Uncertainty in the CIV FWHM
108	DOUBLE	Restframe equivalent width of the whole CIV (Å)
109	DOUBLE	Uncertainty in EW_{CIV}
110	DOUBLE	Power-law slope for the continuum fit for CIV
111	DOUBLE	Uncertainty in α_{CIV}
112	LONG	Number of good pixels for the restframe 1500-1600Å region
113	DOUBLE	Median S/N per pixel for the restframe 1500-1600Å region
114	DOUBLE	Reduced χ^2 for the CIV fit; -1 if not fitted
115	DOUBLE	Velocity shift of broad Hα (kms^{-1}); 3d5 if not measurable
116	DOUBLE	Uncertainty in $V_{H\alpha,broad}$
117	DOUBLE	Velocity shift of narrow Hα (kms^{-1}); 3d5 if not measurable
118	DOUBLE	Uncertainty in $V_{H\alpha,narrow}$
119	DOUBLE	Velocity shift of broad Hβ (kms^{-1}); 3d5 if not measurable
120	DOUBLE	Uncertainty in $V_{H\beta,broad}$
121	DOUBLE	Velocity shift of narrow Hβ (kms^{-1}); 3d5 if not measurable
122	DOUBLE	Uncertainty in $V_{H\beta,narrow}$
123	DOUBLE	Velocity shift of broad MgII (kms^{-1}); 3d5 if not measurable
124	DOUBLE	Uncertainty in $V_{MgII,broad}$
125	DOUBLE	Velocity shift of CIV (kms^{-1}); 3d5 if not measurable
126	DOUBLE	Uncertainty in V_{CIV}
127	DOUBLE	Virial BH mass based on Hβ [MD04, $\log(M_{BH,vir}/M_{\odot})$]
128	DOUBLE	Measurement uncertainty in $\log M_{BH,vir}$ (Hβ, MD04)
129	DOUBLE	Virial BH mass based on Hβ [VP06, $\log(M_{BH,vir}/M_{\odot})$]
130	DOUBLE	Measurement uncertainty in $\log M_{BH,vir}$ (Hβ, VP06)
131	DOUBLE	Virial BH mass based on MgII [MD04, $\log(M_{BH,vir}/M_{\odot})$]
132	DOUBLE	Measurement uncertainty in $\log M_{BH,vir}$ (MgII, MD04)
133	DOUBLE	Virial BH mass based on MgII [VO09, $\log(M_{BH,vir}/M_{\odot})$]
134	DOUBLE	Measurement uncertainty in $\log M_{BH,vir}$ (MgII, VO09)
135	DOUBLE	Virial BH mass based on MgII [S10, $\log(M_{BH,vir}/M_{\odot})$]
136	DOUBLE	Measurement uncertainty in $\log M_{BH,vir}$ (MgII, S10)
137	DOUBLE	Virial BH mass based on CIV [VP06, $\log(M_{BH,vir}/M_{\odot})$]
138	DOUBLE	Measurement uncertainty in $\log M_{BH,vir}$ (CIV, VP06)
139	DOUBLE	The adopted fiducial virial BH mass [$\log(M_{BH,vir}/M_{\odot})$]
140	DOUBLE	Uncertainty in the fiducial virial BH mass (measurement uncertainty only)
141	DOUBLE	Eddington ratio based on the fiducial virial BH mass [$\log(L_{bol}/L_{Edd})$]
142	LONG	Special interest flag
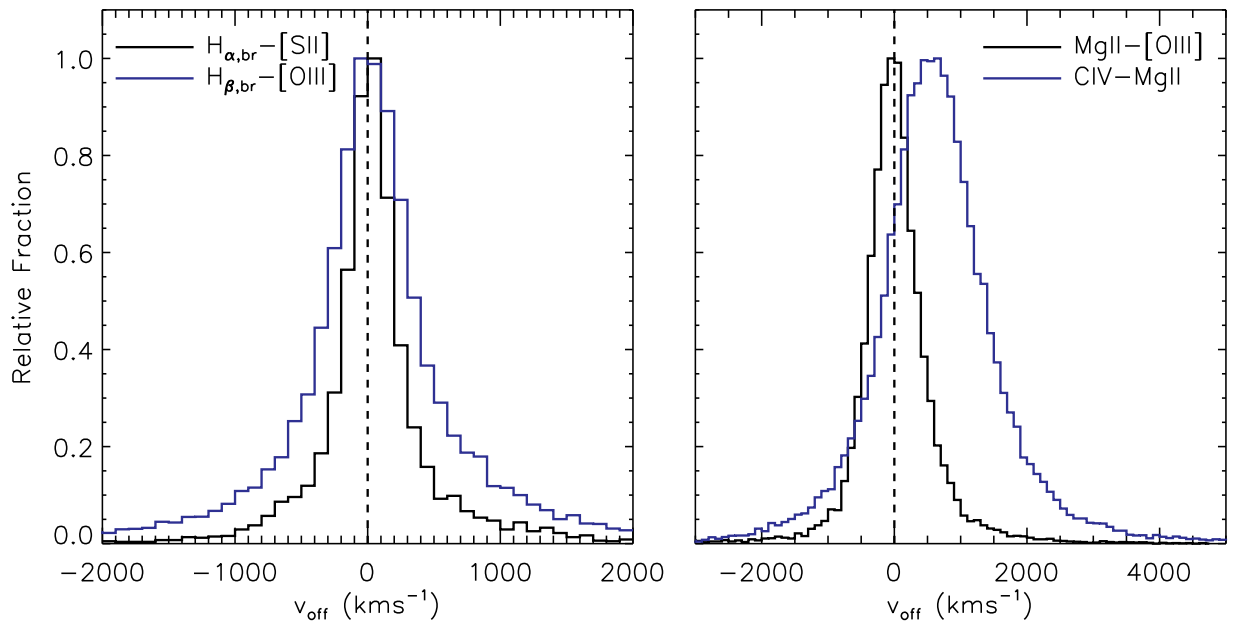
Fig. 17.— Velocity shifts between different pairs of lines. Positive values indicate blueshifts.